

## Article

# Granite Pluton at the Panasqueira Tungsten Deposit, Portugal: Genetic Implications as Revealed from New Geochemical Data

Karel Breiter <sup>1,\*</sup> , Jana Ďurišová <sup>1</sup>, Zuzana Korbelová <sup>1</sup>, Michaela Vašinová Galiová <sup>2,3</sup> and Michaela Hložková <sup>3</sup><sup>1</sup> Institute of Geology, Czech Academy of Sciences, Rozvojová 269, Praha 6, CZ-165 00 Prague, Czech Republic<sup>2</sup> Institute of Chemistry and Technology of Environmental Protection, Faculty of Chemistry, Brno University of Technology, Purkyňova 118, CZ-612 00 Brno, Czech Republic<sup>3</sup> BIC Brno, Purkyňova 125, CZ-612 00 Brno, Czech Republic

\* Correspondence: breiter@gli.cas.cz

**Abstract:** Core samples recovered from exploration boreholes and granite/greisen outcrops at the Panasqueira world-class tungsten deposit in central Portugal were subjected to chemical analyses and petrographic studies. We present a geochemical dataset and the trace element compositions of quartz and micas from a large part of the unexposed Panasqueira granitic pluton. Our data suggest that the hidden granite body is more complicated than previously believed. It consists of a flat cupola of porphyritic granite with only traces of mineralization at Rio and a steep stock of greisenized leucogranite surrounded by a swarm of flat quartz–muscovite veins rich in wolframite between Barroca Grande and Panasqueira. The contents of W (Sn, Nb, Ta) in muscovite markedly drop at a transition from the unmineralized greisen body to quartz veins. The W deposit was formed in three principal stages: (1) intrusion of porphyritic two-mica granite accompanied with local near-contact greisenization and uncommon quartz–wolframite veinlets; (2) intrusion of a more strongly fractionated leucogranite and formation of the cupola and apophyses; (3) circulation of hydrothermal fluids from deeper parts of the granite body into the cupola, greisenization, hydraulic fracturing and opening of flat structures in and outside the cupola and formation of ore veins.



**Citation:** Breiter, K.; Ďurišová, J.; Korbelová, Z.; Vašinová Galiová, M.; Hložková, M. Granite Pluton at the Panasqueira Tungsten Deposit, Portugal: Genetic Implications as Revealed from New Geochemical Data. *Minerals* **2023**, *13*, 163. <https://doi.org/10.3390/min13020163>

Academic Editor: Nuo Li

Received: 15 December 2022

Revised: 9 January 2023

Accepted: 17 January 2023

Published: 22 January 2023



**Copyright:** © 2023 by the authors. Licensee MDPI, Basel, Switzerland. This article is an open access article distributed under the terms and conditions of the Creative Commons Attribution (CC BY) license (<https://creativecommons.org/licenses/by/4.0/>).

**Keywords:** Panasqueira; tungsten deposit; granite; quartz; mica

## 1. Introduction

The Panasqueira world-class vein-type tungsten deposit in central Portugal has been given continuous attention by geologists since its opening in 1898 [1–8]. In 2001, planning a new, professional exploration campaign, the mining company management (then the Avocet Mining plc) organized a revision of all preserved material from archived boreholes [9]. Due to the falling prices of tungsten, however, the campaign was not realized, and the mine was temporarily closed in 2003. After a short break, the mine was reopened, and the subsequent scientific evaluation was very intensive. Significant progress in the study of mineral and chemical compositions of the flat quartz–muscovite–wolframite veins and in deciphering PTX conditions of the origin of mineralization has been achieved, especially during the last decade [10–18]. Nevertheless, relatively little attention was given to the unexposed Panasqueira granite pluton, including the cupola-like greisen body and its importance for vein-type tungsten mineralization [19,20]. This paper partially fills this gap: we decided to publish the results of new laboratory analyses of samples obtained for the 2001 revision, i.e., to publish the first petrological/mineralogical study on this large part of the Panasqueira pluton.

## 2. Geology of the Area

The Panasqueira tungsten deposit occurs in central Portugal, 200 km NE of the capital of Lisbon and 20 km W of Fundao city. In terms of geology, it lies in the Central Iberian Zone (CIZ), which is one of the essential Variscan autochthons, formed by siliciclastic flysch-type sediments of the Douro and Beira groups of Ediacaran to Cambrian age, unconformably overlain by a quartzite-dominated lithology of Ordovician age. During Variscan processes between 359 and 306 Ma, the sediments were slightly metamorphosed (chlorite zone) and deformed and later intruded by three suites of crustal-sourced peraluminous granites (320–290 Ma) [21]. Among these Variscan granites, the Serra Estrela pluton [22], located 15 km NNE of Panasqueira, is the largest but barren one, while Argemela, 14 km E of Panasqueira, is highly fractionated and slightly mineralized with Sn, W and Li [23–26].

The Panasqueira deposit is located within the Beira Group schists, close to a small, completely buried granite pluton, hereafter the Panasqueira pluton. The existence of hidden granite as a probable source of W mineralization was first encountered in 1950 with accidental hits of the uppermost part of the pluton with a mining gallery [1]. Later, the approximate range and depth of the granite were estimated by a series of drill holes (unpublished materials of the mining company, Figure 1, Table A1, Appendix A). Recently, Ribeiro [27] realized a detailed gravity survey around the deposit; his model predicted the thickness of the granite body up to 2 km with deeper roots about 1.5 km SE of Barroca Grande. A combination of gravity modeling with borehole data suggests that the pluton has a N–S-elongated elliptical shape and is roughly 10 × 5 km in size, with its slightly convex upper contact lying in the interval of 200–400 m above sea level.

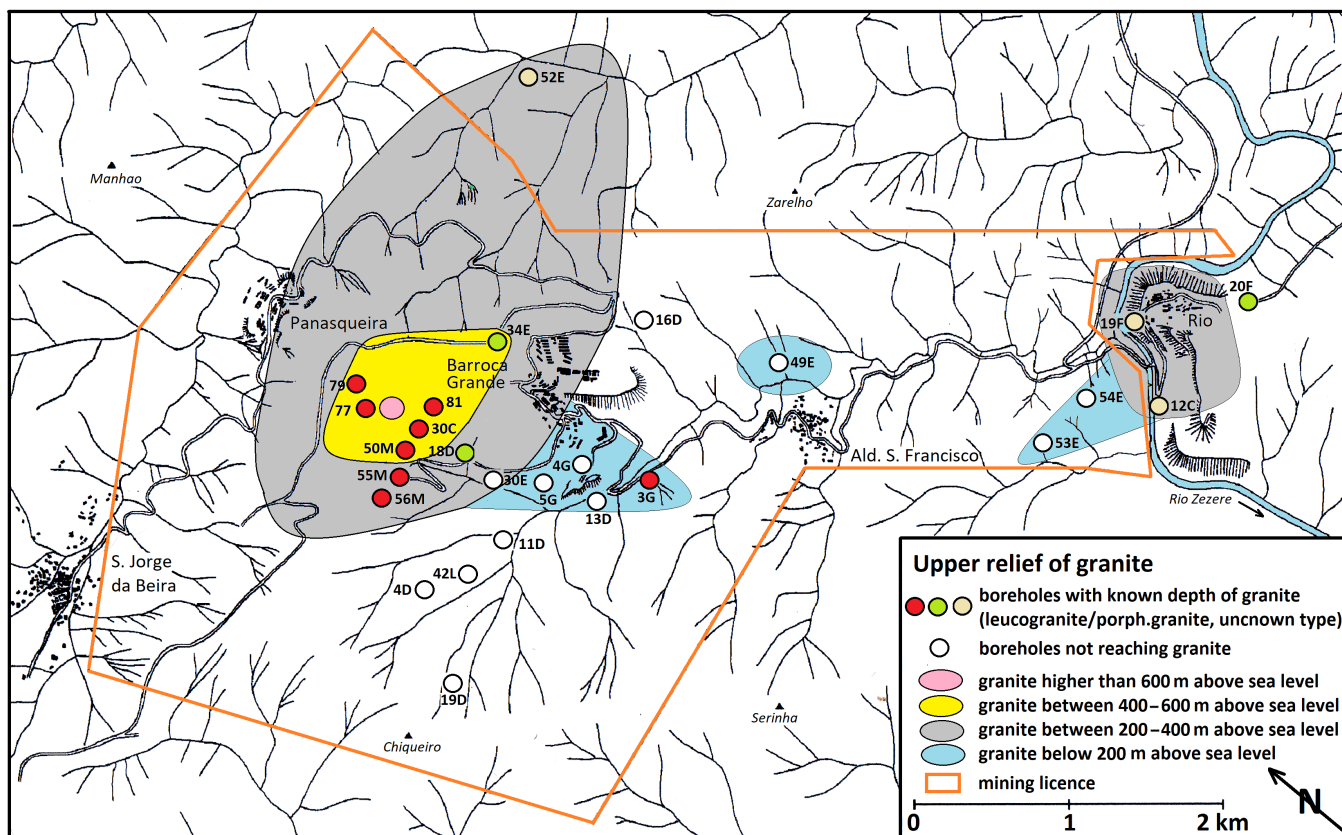


**Figure 1.** A schematic shape of the hidden Panasqueira pluton based on information from the mine and the boreholes. Rem.: black double line—road, black dots—buildings, black-blue double line—river Zezere, thin black lines—streams.

The Panasqueira granite/greisen cupola rises to the level of ca. 650 m above sea level above the generally flat upper contact of the pluton in its NW part (Figure 1). The upper part of the granite cupola was hydrothermally metasomatized to quartz ± muscovite greisen, passing upwards to a nearly pure quartz cap. Locally, a zone of large quartz crystals growing from the contact with schists downwards resembles comb quartz (in the sense Shanon [28]) or quartz-dominated stockscheider from some tin deposits in the Erzgebirge [29]. The greisenized part of the cupola above Level 1 (Figure 2) became inaccessible in 1972 and was described in brief notes only [4]. The whole cupola contains no economically interesting mineralization. Quartz–muscovite veins rich in coarse-grained wolframite, tens of centimeters in thickness, form a generally flat zone within schists above the granite–schist contact, only very rarely crossing the contact between the schists and the cap of the cupola (Figure 2) [4].

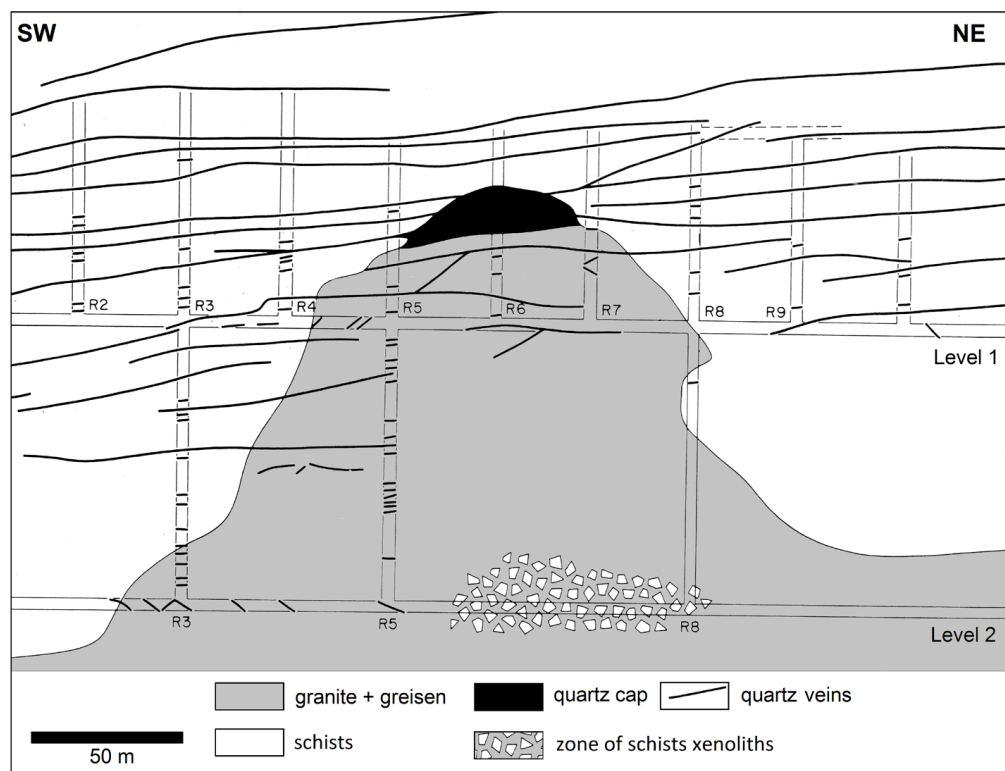


**Figure 2.** A simplified cross-section through the Panasqueira cupola along Panel 4. Vertical and lateral scales are the same. The Rx labels refer to vertical mining workings. Levels 1 and 2 are positioned 620 and 530 m above sea level, respectively. Modified from [1,4].

The second, smaller and flatter pluton elevation at Rio is only poorly known from old boreholes (Figure 1) and is surrounded by only poor indications of quartz–wolframite veinlets.

### 3. Materials and Methods

About 50 studied rock and mineral samples are listed in Table A2 and partly shown in Figure 3.

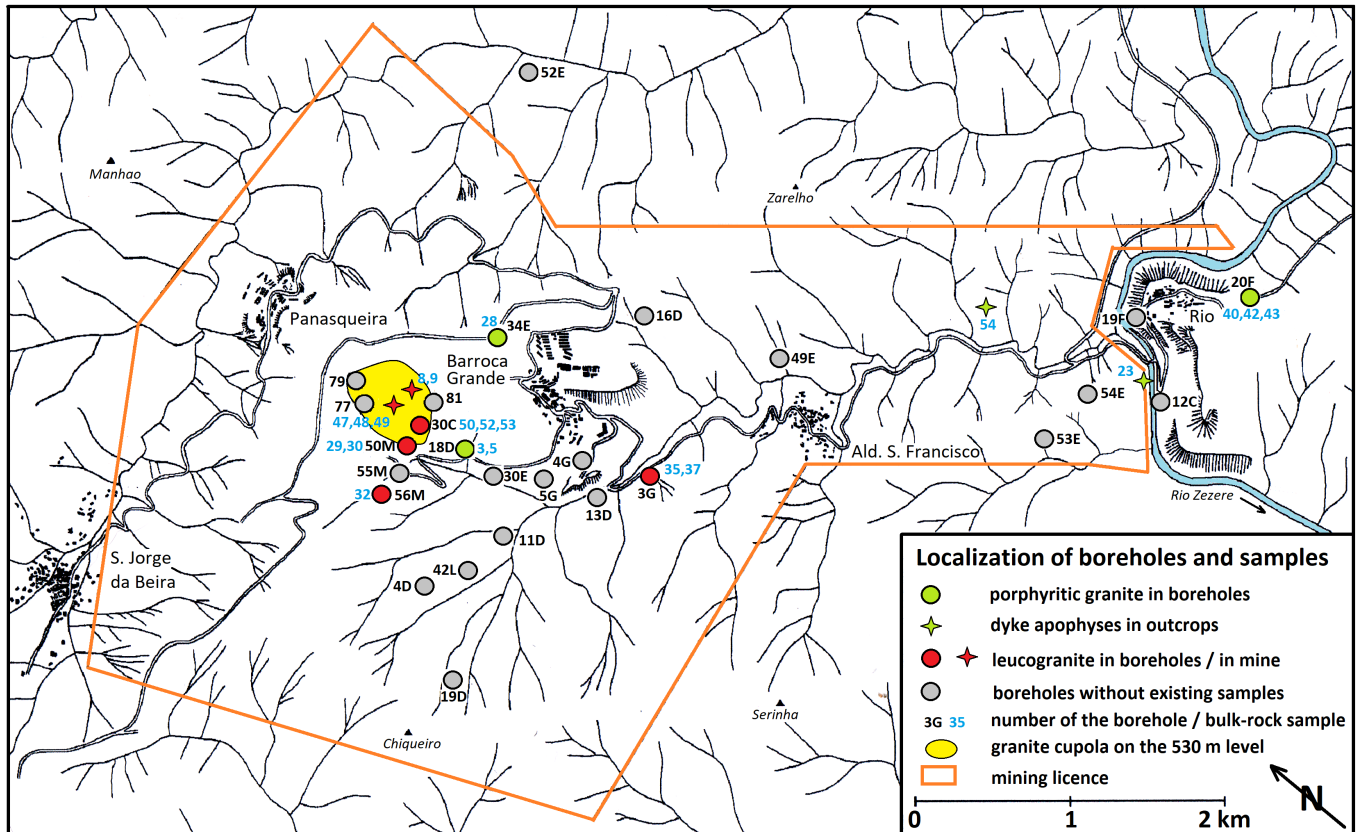


**Figure 3.** Locations of available borehole cores and studied bulk-rock samples. Rem.: black double line—road, black dots—buildings, black-blue double line—river Zezere, thin black lines—streams.

#### 3.1. Bulk-Rock Geochemical Analysis

Bulk-rock major element oxide and trace element contents were determined by ICP-MS in the laboratories of Bureau Veritas Commodities, Vancouver, BC, Canada (<https://commodities.bureauveritas.com>, accessed on 18 January 2023).

#### 3.2. Automated Mineralogy

A TESCAN Integrated Mineral Analyzer (TIMA) based on a TESCAN MIRA FEG-SEM platform in the demonstration facility of its manufacturer, TESCAN ORSAY HOLDING in Brno, Czech Republic, was used for automated mineralogical, modal, and textural analyses. This included the collection of backscattered electron (BSE) and energy dispersive (EDS) data on a regular grid of 10  $\mu\text{m}$  point spacing. A total of 1000 counts per pixel were acquired using the high-resolution mode. An acceleration voltage of 25 kV and a beam current of 10 nA were used during the data acquisition. The individual points were grouped based on a similarity search algorithm, and areas of coherent BSE and EDS data were merged to produce segments (i.e., mineral grains). Individual spectra from points within each segment were summed. Data from each segment were then compared with a classification scheme to identify the mineral and assign its chemistry and density. The results were plotted as a map showing the distribution of minerals within each individual sample [30].

### 3.3. Electron-Microprobe Analyses of Minerals (EMPA)

Major and some minor elements in micas, feldspars, apatite, and zircon were analyzed using a Jeol JXA—8230 electron microprobe housed at the Institute of Geology of the Czech Academy of Sciences, Praha, operated in the wavelength-dispersive mode.

The contents of Si, Ti, Al, Fe, Mn, Zn, Mg, Ca, Na, K, Rb, Cs, and F in micas and the contents of Si, Al, Fe, Ca, Na, K, Rb, and P in feldspars were analyzed at an accelerating voltage of 15 kV, with a beam current of 10 nA and a beam diameter of 2  $\mu\text{m}$ . The following standards were used: F—fluorite, Na—jadeite, Mg—periclase, Al—corundum, Si, Ca—diopside, K—leucite, Ti—rutile, Mn— $\text{Mn}_3\text{O}_4$ , Fe—hematite, Zn—willemite, Rb—RbCl, Cs—pollucite, and P—apatite. The counting times on each peak were optimized for individual elements according to their expected concentrations (20–60 s), and half that time was used to obtain background counts. X-ray lines and background offsets were selected to minimize interference.

The composition of apatite was determined using a 15 keV acceleration voltage, 10 nA beam current, and 2  $\mu\text{m}$  beam diameter. The concentrations of the following elements were measured (spectral line, standard, and spectrometer crystal for analyzed element): Ca  $\text{K}\alpha$  (apatite, PETJ), P  $\text{K}\alpha$  (apatite, PETL), F  $\text{K}\alpha$  (fluorite, LDE1L), Mn  $\text{K}\alpha$  (rhodonite, LIFH), Fe  $\text{K}\alpha$  (hematite, LIFH), Sr  $\text{L}\alpha$  (celestite, PETL), Mg  $\text{K}\alpha$  (periclase, TAPL). Counting times on peaks were 20 s for: Ca, P, Mn, Fe, Sr, and Mg; 30 s for F.

Elemental abundances of F, Al, Si, P, S, Ca, Sc, Ti, Mn, Fe, As, Y, Zr, Nb, Dy, Er, Yb, Hf, W, Pb, Bi, U, and Th in zircon were determined at an accelerating voltage of 15 kV and a beam current of 15 nA and with a beam diameter ranging from 1 to 2  $\mu\text{m}$ . The counting times on each peak were optimized for individual elements according to their expected concentrations (20–60 s), and half that time was used to obtain background counts. Again, X-ray lines and background offsets were selected to minimize interference. The following reference materials were used: fluorite (F), corundum (Al), quartz (Si), apatite (P), barite (S), diopside (Ca), metallic Sc (Sc), rutile (Ti),  $\text{Mn}_3\text{O}_4$  (Mn), hematite (Fe), gallium arsenide (As), synthetic cubic zirconia (Y, Zr), metallic Nb (Nb), REE glass standard Dy\_Ho\_Er (Dy, Er), REE glass standard Nd\_Sm\_Yb\_Lu (Yb), metallic hafnium (Hf), metallic W (W), crocoite (Pb), metallic Bi (Bi), metallic Th (Th), and metallic U (U).

In all minerals, raw data were processed using the  $\phi\rho Z$  correction procedure (XPP method metal/oxide was applied). Empirically determined correction factors were applied to the overlapping X-ray lines. Empirical formulae were calculated on the basis of appropriate amounts of atoms of oxygen in a formula unit (apfu).

### 3.4. Trace Elements in Quartz

The contents of Al, B, Be, Fe, Ge, Li, Mn, P, Rb, Sn, Sr, and Ti in quartz were determined using laser-ablation inductively coupled mass spectrometry (LA-ICP-MS) at the Institute of Geology of the Czech Academy of Sciences. The system involved a Thermo-Finnigan Element 2 sector field mass spectrometer coupled with an Analyte Excite 193 nm excimer Laser (Photon Machines). The laser was fired at a repetition rate of 10 Hz, with a laser fluence of 4–5  $\text{J}/\text{cm}^2$  and a beam size of 100  $\mu\text{m}$ . The ablated material was transported by a high-purity He gas from the laser ablation cell. Time-resolved signal data were processed using the Glitter software (<http://www.glitter-gemoc.com/> (accessed on January 18, 2023)). The isotope  $^{29}\text{Si}$  was used as the internal standard based on the assumption that the analyzed quartz contains 99.95 wt.%  $\text{SiO}_2$ . Data were calibrated against the external standard of synthetic silicate glass NIST SRM 612 using the reference values published by [31]; for more details, see [32]. To monitor the reproducibility of the standardization method, we analyzed NIST SRM 1830 as an unknown along with each set of quartz samples. The relative deviations between the measured and reference concentrations [33] were better than 10% for all elements except Al and Ge, which were underestimated by 20% and 16%, respectively.

### 3.5. Trace Elements in Mica

The contents of trace elements Li, Sc, Ti, Mn, Fe, Ga, Ge, Rb, Nb, In, Sn, Cs, Ta, W, and Tl in mica samples were determined using LA-ICP-MS instrumentation housed at the Faculty of Chemistry, Brno University of Technology and BIC Brno. This consists of an ArF\* excimer laser ablation system Analyte Excite+ (Teledyne CETAC Technologies, Omaha, NE, USA) emitting the laser beam at a wavelength of 193 nm and quadrupole ICP mass spectrometer Agilent 7900 (Agilent Technologies, Inc., Santa Clara, CA, USA). The laser ablation system, Analyte Excite+, has a 2-Volume HelEx II Cell, and the ablated material was carried using helium carrier gas (0.5 + 0.3 l/min) and mixed with argon (~1 l/min) prior to the torch. The sample surface of individual spots was ablated by a 50 µm-laser beam diameter with a fluence of 3 J/cm<sup>2</sup> and a 10 Hz repetition rate. Each spot analysis incorporated 40 s of background (Ar–He gas blank) followed by 35 s of data acquisition from the sample. The monitored isotopes were as follows: <sup>7</sup>Li<sup>+</sup>, <sup>27</sup>Al<sup>+</sup>, <sup>28</sup>Si<sup>+</sup>, <sup>39</sup>K<sup>+</sup>, <sup>45</sup>Sc<sup>+</sup>, <sup>47,49</sup>Ti<sup>+</sup>, <sup>55</sup>Mn<sup>+</sup>, <sup>56,57</sup>Fe<sup>+</sup>, <sup>69</sup>Ga<sup>+</sup>, <sup>72,73</sup>Ge<sup>+</sup>, <sup>85</sup>Rb<sup>+</sup>, <sup>93</sup>Nb<sup>+</sup>, <sup>113,115</sup>In<sup>+</sup>, <sup>116,117,118,119</sup>Sn<sup>+</sup>, <sup>133</sup>Cs<sup>+</sup>, <sup>181</sup>Ta<sup>+</sup>, <sup>182,183</sup>W<sup>+</sup>, <sup>203,205</sup>Tl<sup>+</sup>, <sup>232</sup>Th<sup>+</sup>, <sup>238</sup>U<sup>+</sup>. In the case of several elements (Ti, Fe, Ge, In, Sn, W, and Tl), two or more isotopes were measured to identify and exclude the presence of possible spectral interferences. The limits of detection were calculated as  $3 \times SD/b$  where *SD* means the standard deviation of the He–Ar gas blank and *b* is the sensitivity. The average detection limits under the operating conditions were as follows: 1.7 ppm Li; 7.1 ppm Al; 440 ppm Si; 13 ppm K; 0.23 ppm Sc; 0.63 ppm Ti; 0.41 ppm Mn; 1.8 ppm Fe; 0.02 ppm Ga; 0.28 ppm Ge; 0.32 ppm Rb; 0.01 ppm Nb; 0.08 ppm In; 0.13 ppm Sn; 0.02 ppm Cs; 0.01 ppm Ta; 0.01 ppm W; 0.02 ppm Tl; 0.01 ppm Th; and 0.01 ppm U. Accuracy control was performed by repeated measurements of an in-house mica reference sample. The ICP mass spectrometer was tuned using SRM NIST 612 with respect to the maximum sensitivity and minimal doubly charged ions, oxide formations (<sup>248</sup>ThO<sup>+</sup>/<sup>232</sup>Th<sup>+</sup> < 1%), and mass response <sup>238</sup>U<sup>+</sup>/<sup>232</sup>Th<sup>+</sup> ~1. The potential polyatomic interferences were minimized via a collision cell (He 1 ml/min). The elemental contents were calibrated using artificial glass standards SRM NIST 610 and 612, and Si and Al as internal reference elements after baseline correction and integration of the peak area using HDIP software (Teledyne CETAC Technologies, Omaha, NE, USA).

## 4. Results

### 4.1. Textures of Granites, Greisens, and Quartz Veins

In boreholes, two-mica porphyritic granite forms the majority of the unexposed Panasqueira pluton. It contains porphyroclasts of subhedral quartz (up to 5 mm in diameter) and zoned plagioclase (altered oligoclase cores with albitic rims up to 10 × 4 mm in size) and smaller flakes of biotite embedded in a fine-grained groundmass of quartz, albite, poikilitic K-feldspar, and late muscovite (Table 1, Figure 4a). Biotite grains are strongly or partially altered to aggregates of phengitic muscovite + hematite. The main accessory phases are apatite, hematite, rutile, zircon, and monazite; clay minerals are common in the altered domains.

**Table 1.** Modal composition according to TIMA (vol.%).

Rock Type Sample	Porphyr. Granite #5	Leucogranite #37	Greisen #10
Quartz	35.61	32.37	52.25
Albite	28.67	38.47	0.38
K-feldspar	11.57	12.93	0.11
Muscovite	7.53	13.33	31.78
Fe-mica	14.71	1.92	8.68
Apatite	0.56	0.76	0.49
Kaolinite	0.35	0.13	0.05
Fe-sulfides			6.21
Hematite	0.62		0.55
Topaz		0.01	

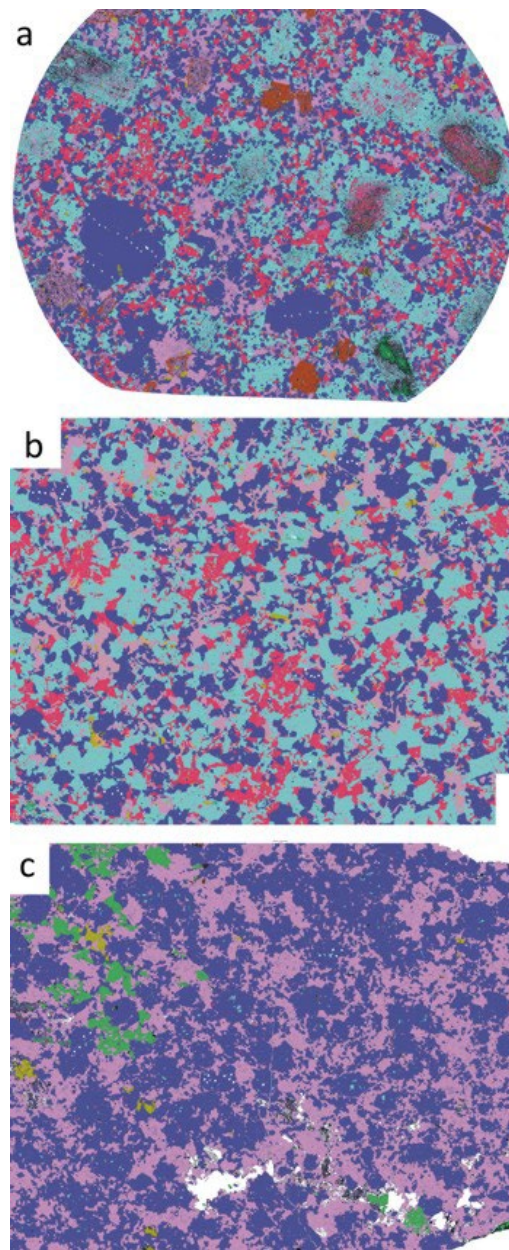


**Figure 4.** Textures of the main rock types visualized by automated mineralogy (TIMA): (a) porphyritic granite (#5); (b) leucogranite (#37); (c) greisen (#10). Width of all samples is 4 cm. Dark blue—quartz; red—K-feldspar; light blue—plagioclase; green—sulfides; yellow—apatite; brown—biotite; pink—muscovite; white—cavity.

Leucogranite occurs exclusively within the cupola and in borehole 3G, situated ca. 0.5 km south of Barroca Grande (Figure 3). It is composed of quartz, albite, K-feldspar, and variable quantities of muscovite (Figure 4b). Apatite is common; rutile, topaz, zircon, and monazite are present as accessory phases.

In the cupola, leucogranite is variably greisenized, i.e., albite and K-feldspar are replaced by newly formed hydrothermal quartz and muscovite with a subordinate amount of apatite, topaz, and kaolinite. Locally, small remnants of feldspars are embedded in quartz. Sulfides (pyrite, arsenopyrite) are common, cassiterite is accessory, and wolframite is very scarce (Figure 4c).

Wolframite-bearing quartz veins (<1 m thick), located mainly in the western exocontact of the cupola, are flat-lying. These veins are usually rimmed by a zone of coarse-grained muscovite, several centimeters thick, growing perpendicular to the contact plane inside the opening space. This muscovite rim thickness correlated negatively with the width of the veins. The inner parts of the veins are dominated by milky quartz rich in wolframite (columns max. 20 cm in size) and less abundant sulfides. Apatite and carbonates are subordinate; tourmaline and rutile appear along the contact between the vein and the schists.

#### 4.2. Bulk-Rock Chemical Composition of Granites and Greisens

The chemical compositions of the two granite types, i.e., porphyritic granite and leucogranite, are similar in their major element contents but clearly differ in their trace element contents. The composition of greisens differs significantly (Table 2, Figure 5). The contents of SiO<sub>2</sub> increase from 71 to 74 wt.% in porphyritic granite to 73–75 wt.% in leucogranite and reach up to 80 wt.% in greisen. The contents of Al range between 13.5 and 15.5 wt.% in granites but decrease to about 12 wt.% due to greisenization (Figure 5a). All granite varieties of the Panasqueira pluton are distinctly peraluminous; their alumina saturation index (ASI) is 1.3–1.8 in porphyritic and leucocratic granites and 1.5–1.9 in greisenized granites and greisens.

**Table 2.** Bulk-rock chemical composition of the studied granites and greisens (wt.%, traces in ppm).

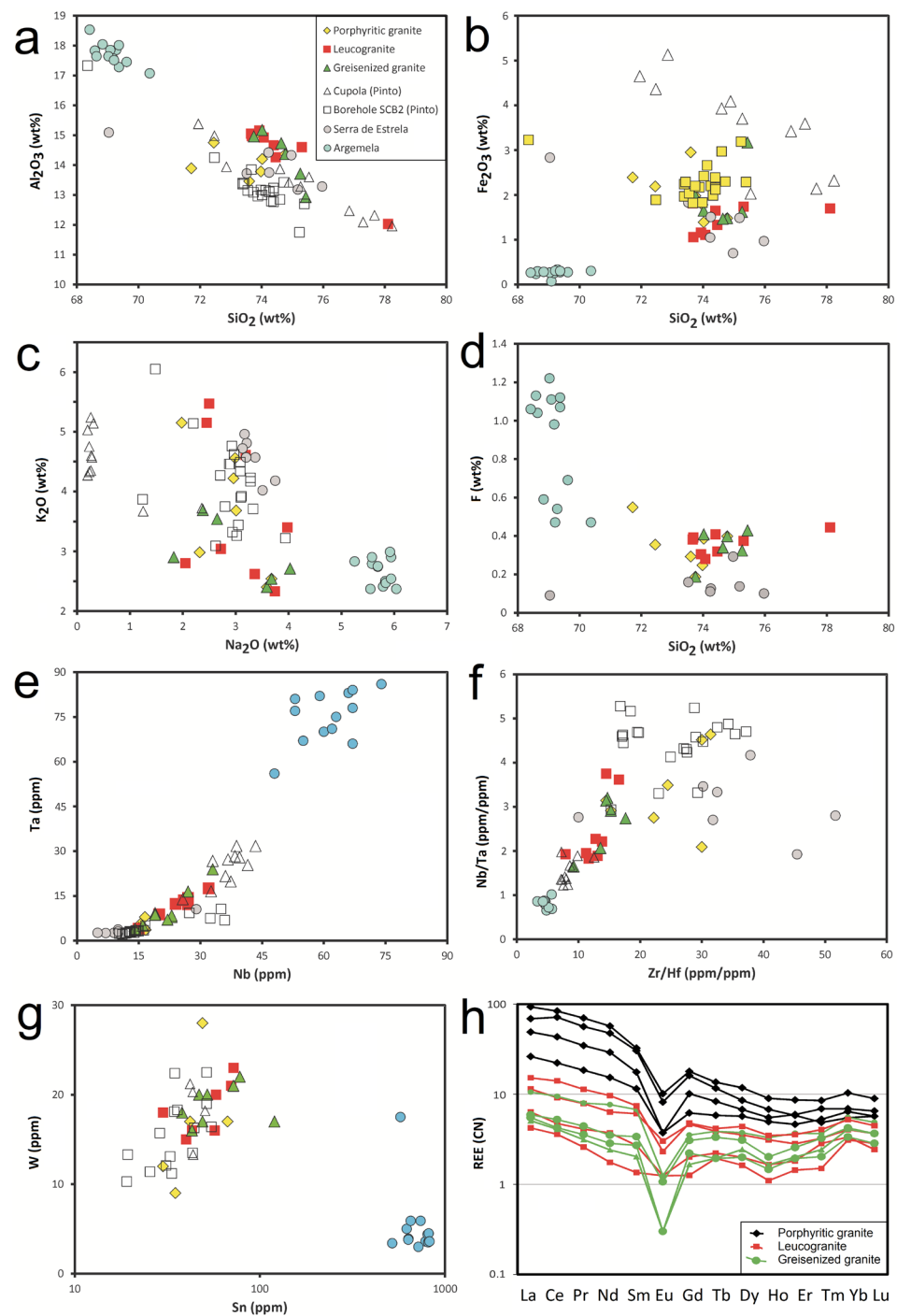
Sample	5	52	43	8	32	37	47	9	48
Rock	Porphyritic Granite			Leucogranite			Greisenized Granite		
SiO <sub>2</sub>	72.45	71.72	73.60	73.93	75.31	73.68	74.46	74.02	75.44
TiO <sub>2</sub>	0.33	0.25	0.16	0.01	0.01	0.04	0.03	0.02	0.03
Al <sub>2</sub> O <sub>3</sub>	14.75	13.89	13.46	15.16	14.60	14.97	14.26	15.17	12.93
Fe <sub>2</sub> O <sub>3</sub> tot	2.19	2.39	2.95	1.16	1.74	1.06	1.33	1.65	3.17
MnO	0.04	0.05	0.03	0.02	0.03	0.02	0.03	0.03	0.04
MgO	0.43	0.38	0.42	0.07	0.09	0.07	0.09	0.11	0.27
CaO	0.50	0.66	0.52	0.24	0.24	0.66	0.34	0.28	0.37
Na <sub>2</sub> O	2.99	1.98	2.32	2.50	2.72	3.98	2.45	2.65	1.83
K <sub>2</sub> O	4.56	5.15	2.98	5.47	3.04	3.40	5.15	3.54	2.90
P <sub>2</sub> O <sub>5</sub>	0.32	0.52	0.36	0.19	0.19	0.59	0.27	0.20	0.22
C	0.10	0.10	0.16	−0.01	0.05	0.01	0.01	0.02	0.14
S	0.02	0.17	0.70	0.02	0.16	0.02	0.11	0.03	0.68
LOI	1.40	3.00	3.10	1.20	2.00	1.60	1.40	2.30	2.50
F	0.35	0.55	0.29	0.31	0.37	0.39	0.32	0.41	0.43
<b>Total</b>	99.99	100.02	99.90	99.96	99.98	99.99	99.82	99.98	99.70
As	117	27	452	1200	367	113	531	369	5390
B	15	17	15	24	24	21	19	30	22
Ba	226	176	29	75	18	8	68	42	32
Bi	3.5	1.2	23.2	7.3	15.1	5	10	4.4	42.9
Cs	35	37	19	28	33	23	23	35	26
Cu	21	30	249	16	132	5	108	15	468
Ga	26	26	34	29	36	35	30	35	31
Hf	3.5	3.1	2.9	3.3	3.2	2.1	1.8	2.6	1.4
Nb	17	17	15	26	24	27	20	27	19
Pb	21	4	4	46	15	4	19	20	48
Rb	626	669	430	793	721	743	717	772	593
Sc	4	3	3	<1	−1	3	2	<1	1
Sn	30	67	42	43	70	30	57	78	72

Table 2. Cont.

Sample	5	52	43	8	32	37	47	9	48
Rock	Porphyritic Granite			Leucogranite			Greisenized Granite		
Sr	42	54	15	21	18	82	19	19	12
Ta	3.6	7.9	4.3	13.5	12.3	12.2	8.8	16.4	9.2
Th	12.8	12.2	6.4	1.5	1.0	2.0	1.1	1.2	0.8
Tl	1.6	2.0	0.8	2.2	1.4	1.5	1.7	1.7	1.4
U	17	25	30	20	27	56	26	18	18
V	14	6	6	<5	<5	<5	<5	<5	<5
W	12	17	17	16	21	18	16	22	21
Y	13.8	9.9	10.3	0.6	0.9	5.4	3.2	0.8	2.8
Zn	148	203	7	30	15	5	235	63	291
Zr	110	93	71	26	36	29	23	24	19
La	22.1	16.3	9.3	0.6	−0.5	2.7	1.5	0.7	1.3
Ce	51.3	43.8	21.8	0.9	0.5	5.6	2.9	0.9	2.6
Pr	6.49	5.22	2.71	0.10	0.08	0.73	0.38	0.12	0.33
Nd	26.0	21.7	10.7	<0.4	<0.4	2.9	1.7	<0.4	1.3
Sm	4.8	4.5	2.6	−0.1	−0.1	0.9	0.4	<0.1	0.4
Eu	0.57	0.46	0.17	<0.05	<0.05	0.17	0.07	<0.05	<0.05
Gd	3.56	3.20	1.98	<0.05	0.07	0.92	0.40	0.11	0.44
Tb	0.49	0.42	0.33	0.01	0.01	0.14	0.08	0.02	0.07
Dy	2.90	2.10	1.90	0.08	0.15	0.87	0.49	0.10	0.49
Ho	0.49	0.37	0.36	<0.05	−0.05	0.17	0.09	−0.05	0.08
Er	1.38	0.93	1.02	0.06	0.09	0.45	0.29	0.06	0.31
Tm	0.21	0.12	0.18	<0.05	<0.05	0.08	0.07	<0.05	0.05
Yb	1.66	0.88	1.29	0.10	0.30	0.65	0.54	0.15	0.54
Lu	0.22	0.14	0.16	0.02	0.04	0.09	0.06	0.02	0.07
ASI	1.37	1.38	1.68	1.45	1.78	1.31	1.39	1.74	1.89
Zr/Hf	31.4	30.0	24.5	7.9	11.3	13.8	12.8	9.2	13.6
Nb/Ta	4.6	2.1	3.5	1.9	2.0	2.2	2.3	1.6	2.1

The contents of Mg and Fe slightly decrease from porphyritic granite to leucogranite but somewhat increase in the greisenized rocks (Figure 5b). The contents of alkalis in granites vary broadly: K<sub>2</sub>O contents range between 2.5 and 5.5 wt.%, and Na<sub>2</sub>O contents between 2 and 4 wt.%. During greisenization, i.e., the destruction of feldspars, Na<sub>2</sub>O contents decrease substantially while K contents remain mostly stable, with K being incorporated in newly formed muscovite (Figure 5c). The contents of phosphorus and fluorine vary in all rock types: 0.25–0.5 wt.% P<sub>2</sub>O<sub>5</sub> and 0.2–0.4 wt.% F (Figure 5d).

Among the trace elements, only a small increase in Rb was encountered from 430 to 660 ppm in porphyritic granite to 700 to 800 ppm in leucogranite. The Rb contents in the analyzed greisen samples are intermediate between those in the leucogranite and porphyritic granite samples. HFSE elements Nb and Ta, much like Zr and Hf, are relatively less mobile elements; their contents and especially their ratios are reliable indicators of magmatic fractionation. An increase in the Nb and Ta contents and a decrease in the Nb/Ta value from the porphyritic to leucocratic granites can be attributed to magmatic fractionation. The contents of Nb and Ta and their ratio in greisenized rocks are similar to their magmatic precursors (Figure 5f). The contents of Zr decrease from 50 to 110 ppm to 20 to 40 ppm from porphyritic to leucocratic granites at similar Hf contents (about 3 ppm), which implies a decrease in the Zr/Hf value from 30 to <10. The Nb/Ta and Zr/Hf values define a clear evolutionary trend from porphyritic granite to leucogranite (Figure 5g).



**Figure 5.** Bulk chemical composition of granites from Panasqueira: (a)  $SiO_2$  vs.  $Al_2O_3$ ; (b)  $SiO_2$  vs.  $Fe_2O_3$ tot; (c)  $Na_2O$  vs.  $K_2O$ ; (d)  $SiO_2$  vs. F; (e) Nb vs. Ta; (f) Zr/Hf vs. Nb/Ta; (g) Sn vs. W; (h) distribution curves of chondrite-normalized REEs [34]. Analyses from Panasqueira made by Pinto [20] and compositions of typical samples from the Serra Estrela pluton [22] and Argemela stock [23] are shown in (a–g) for comparison.

The contents of tin and tungsten vary, showing no correlation with rock types or any other elements: they mostly lie between 30 and 70 ppm Sn and 15 and 25 ppm W.

The absolute contents of REEs vary significantly not only among rock types but also among samples of a particular rock type (Figure 5h). The distribution curve of REE in porphyritic granite has a right-falling shape with a prominent negative Eu anomaly, typical for peraluminous granites. The total REE contents are 36–122 ppm. In leucogranite

and greisens, REE contents (1–8 ppm in total) are lower, especially those of LREE. The distribution curve is flatter. The intensity of the tetrad effect is variable: the first tetrad is better visible in the porphyritic granite, while the second tetrad is the most intensive in greisens.

The contents of Th decrease from porphyritic granite to leucogranite and greisen (12→1 ppm), while contents of U are variable but similar in all rock types in the range of 20–30 ppm. Local enrichment in some other elements includes max. 5000 ppm As, 43 ppm Bi, 468 ppm Cu, and 290 ppm Zn.

#### 4.3. Quartz

We performed about 300 LA-ICP-MS spot analyses. The results are presented in diagrams in Figure 6, and chemical compositions along profiles across typical quartz crystals are listed in Table 3 and visualized in Figure 7.

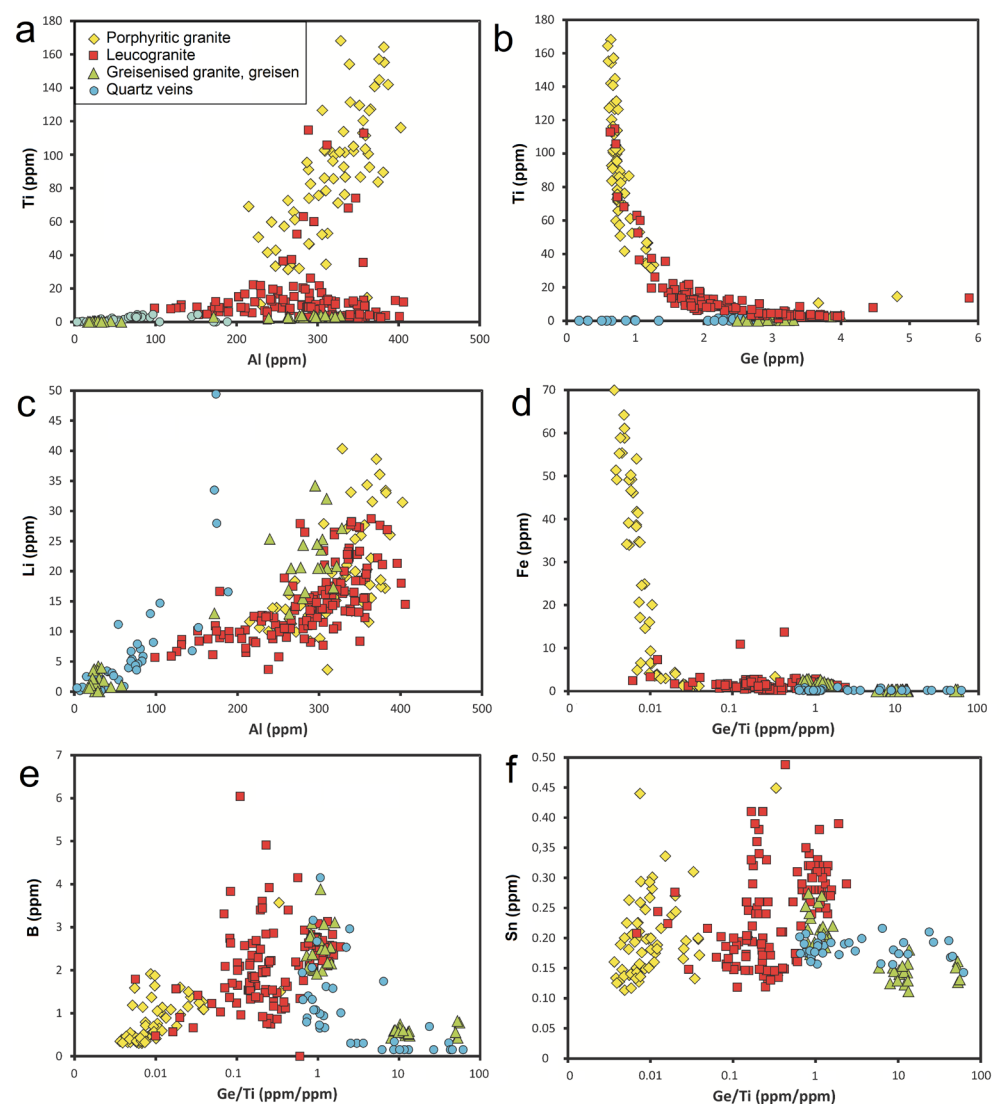


**Figure 6.** Contents of trace elements in quartz: (a) Al vs. Ti; (b) Ge vs. Ti; (c) Al vs. Li; (d) Ge/Ti vs. Fe; (e) Ge/Ti vs. B; (f) Ge/Ti vs. Sn.

**Table 3.** Contents of trace elements in typical quartz crystals in ppm (LA-ICP-MS data). Empty cell—below detection limit.

Sample	43					47					9						Lim. Det.		
Rock	Porphyritic Granite					Leucogranite					Greisenized Granite								
Spot	17	18	19	20	21	38	39	40	41	42	53	54	55	56	57	58	59	60	
Li	10.6	15	15.7	14.9	13.9	8.9	10.4	10.9	11	6.1	23.3	27.7	27.6	28.7	18.4	28.2	26.9	21.1	0.2
Be	0.2	0.05	0.05	0.05	0.11	0.14	0.16	0.05	0.12	0.05	0.17	0.16	0.16	0.12	0.12	0.16	0.18	0.19	0.05
B	1.1	0.6	0.3	0.3	0.6	1.6	2.5	1.5	1.5	1.1	2.6	2.5	2.4	2.6		2.9	2.3	2.8	0.2
Ge	0.78	0.79	0.73	0.67	0.72	2.56	1.95	1.97	1.89	2.44	3.76	3.69	3.4	3.15	2.8	3.08	3.56	3.95	0.1
Rb	0.33	0.45	0.55	0.51	0.23	0.32	1.14	0.73	0.65	0.09	0.48	0.69	0.83	0.71	0.67	0.85	0.69	0.58	0.05
Sn		0.15	0.14	0.16	0.18	0.15	0.25	0.18	0.16	0.13	0.27	0.3	0.31	0.35	0.31	0.29	0.3	0.51	0.05
Al	227	291	319	289	243	178	281	287	256	170	350	339	375	364	352	340	384	378	5
P	5.0	4.9	5.1	5.5	5.0	5.5	6.3	6.6	5.5	4.4	11.4	11.7	11.0	11.4	11.8	10.6	10.9	12.7	1
Ti	51	83	96	91	60	6.1	9.9	8.8	8.3	6.9	2.5	3.0	3.2	4.1	4.7	4.5	3.9	2.6	0.2
Mn	0.3	0.6	0.6	0.5	0.4	0.1	0.4	0.3	0.9	0.1									0.5
Fe	3.0				3.7	0.7	2.4	1.9	1.9	0.8	1.7	1.8	2.8	2.0	3.0	1.9	2.1	1.7	0.2

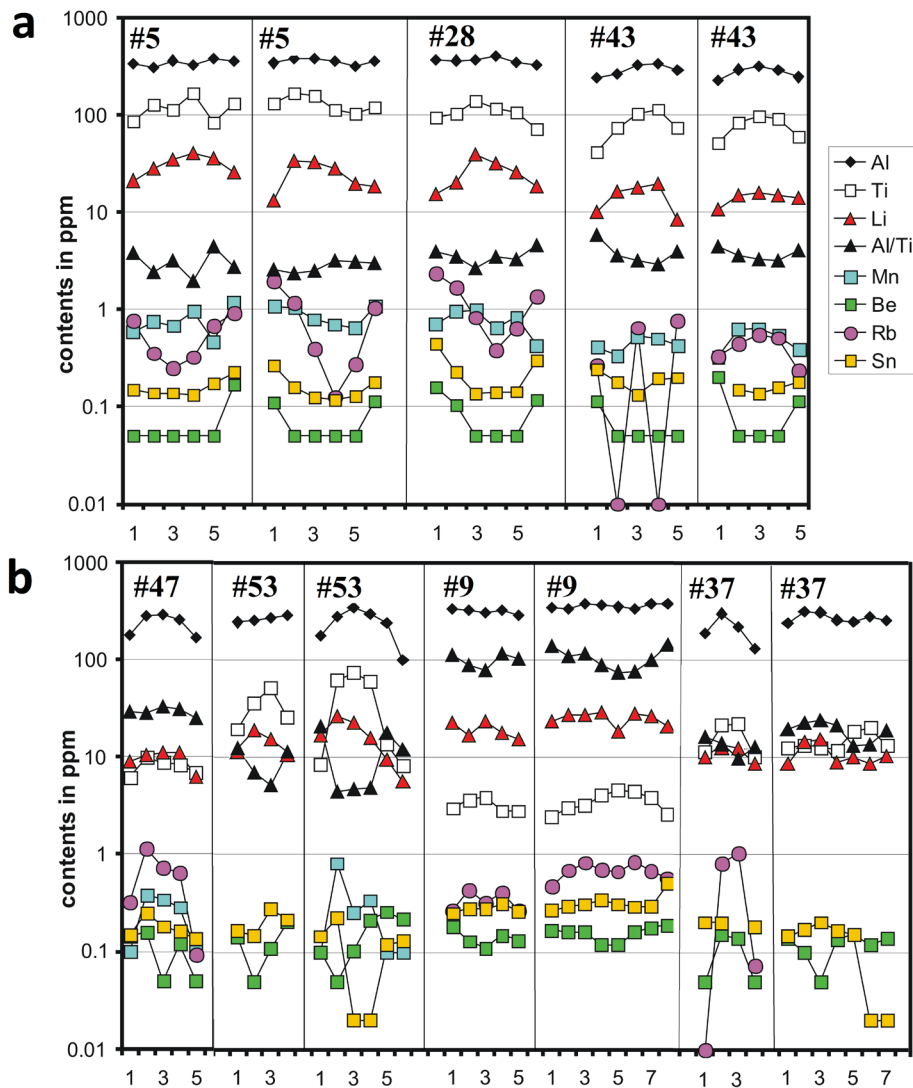


**Figure 7.** Chemical compositions along profiles across selected quartz grains: (a) porphyritic granite (samples Nos. 5, 28, 43); (b) leucogranite (samples Nos. 47, 53) and greisenized granite (Nos. 9, 37).

Porphyritic granite contains early well-shaped quartz phenocrysts, up to 5 mm across, with indistinct cathodoluminescence (CL) zoning, and late fine anhedral grains (0.X mm) forming—together with K-feldspar—groundmass surrounding plagioclase and quartz phenocrysts. Quartz grains in leucogranite are mostly anhedral, 1–2 mm in size, and with no CL, crystallized after albite. Greisenized granite passing to greisen contains 50–90 vol.% of quartz. Its quartz grains are anhedral, 0.X to X mm in size, with no CL; these grains combine relicts of primary magmatic quartz with younger hydrothermal quartz formed during greisenization; these two quartz varieties can be distinguished only by local chemical analysis.

Magmatic quartz from porphyritic granite significantly differs from that from leucogranite in the contents of some trace elements, being richer in Al (200–400 vs. 100–350 ppm), Ti (40–170 vs. mostly 10–30 ppm), Fe (3–70 vs. <5 ppm) and Li (10–40 vs. 5–20 ppm), but poorer in Ge (0.5–1.5 vs. mostly 1–3 ppm) and B (<2 vs. 1–4 ppm) (Figure 6).

Hydrothermal quartz from greisen and the quartz–muscovite veins is comparatively poor in Ti and Fe (<2 ppm). Greisen quartz differs from vein quartz, especially in the contents of Al (240–340 vs. mostly < 110 ppm), Li (mostly 15–35 vs. mostly <10 ppm), and Ge (mostly > 3 vs. mostly < 3 ppm). The relatively higher values from greisen quartz represent relicts of magmatic quartz, and the lower values reflect hydrothermal overgrowth or re-equilibration.

Some magmatic quartz grains show chemical zoning (Figure 7). The contents of Al, Ti, and Li usually decrease from core to rims in quartz from both porphyritic and leucocratic granites, following the general fractional trend, while the contents of Sn and Be increase. The behavior of Fe, Mn, Rb, and Ge is variable; nevertheless, both proposed indicators of fractionation, i.e., the Al/Ti and Ge/Ti values [35], increase towards the rims.

#### 4.4. Micas

About 230 EMP+LA-ICP-MS spot analyses of micas were performed. Mean compositions of typical mica grains (means of 4–5 spots) are given in Table 4, and relations among some elements are visualized in Figure 8. Porphyritic granite contains primarily two micas—biotite and muscovite, but part of the biotite grains were changed to secondary muscovite. The composition of biotite corresponds to Li-enriched siderophyllite, while magmatic muscovite occupies a field between muscovite *s.s.* and phengite (Table 4, Figure 8a). Some grains of secondary muscovite, relatively rich in Ti, Fe, and Mg, and poor in Li and Rb, fall into the compositional gap between muscovite and siderophyllite defined by [36], reflecting their origin via muscovitization of biotite. The composition of muscovite from leucogranite, greisen, and ore veins varies from muscovite to phengite. Muscovite grains from all rock types have often thin Fe-enriched rims resulting from equilibration with late fluids.

The contents of Li are generally low, not exceeding 3400 ppm Li in biotite and 4000 ppm (0.39 apfu Li) in muscovite. In both micas, Li positively correlates with Fe (Figure 8b), indicating a  $\text{Li}^+ + \text{Fe}^{2+} \Leftrightarrow \text{Al}^{3+}$  substitution. The contents of Rb generally correlate with Li and F as a result of the degree of fractionation of parental melt. The Rb/Li ratio is slightly <1 in biotite but distinctly >1 in muscovite (Figure 8d).

The contents of Mg range from 3.6 to 4.0 wt.% MgO (#Fe = 75–78) in biotite and mostly 0.5–0.8 wt.% MgO (#Fe = 60–90) in muscovite from granites and quartz veins and <0.1 wt.% MgO (#Fe = 90–100) in muscovite from greisenized granites and greisens. The contents of Mn do not exceed 1200 ppm in all types of muscovite and ca. 4000 ppm in biotite with a stable Mn/Fe ratio of 1:40 (Figure 8c).

**Table 4.** Chemical composition (wt.%, EMPA), empirical formulae, and contents of trace elements (ppm, LA-ICP-MS) of micas. Means of 20–25 spot analyses are tabled.

Sample		5	28	43	8	53	9	10	11	20	
Rock		Porphyritic Granite			Leucogranite		Greisenized Leucogranite		Ore Vein		
SiO <sub>2</sub>	%	36.01	45.98	46.74	46.78	46.60	47.19	46.36	46.18	46.79	46.59
TiO <sub>2</sub>	%	2.57	0.38	0.48	0.40	0.04	0.24	0.10	0.07	0.06	0.16
Al <sub>2</sub> O <sub>3</sub>	%	19.06	34.30	32.01	32.45	33.22	33.89	32.91	33.19	32.26	32.93
FeO	%	22.36	2.57	4.06	2.95	4.29	2.41	4.05	3.99	4.41	3.89
MnO	%	0.52	0.07	0.08	0.05	0.08	0.05	0.08	0.07	0.10	0.07
MgO	%	3.97	0.93	0.79	0.77	0.09	0.63	0.10	0.04	0.10	0.66
ZnO	%	0.17	0.03	0.05	0.04	0.03	0.03	0.06	0.05	0.05	0.04
CaO	%	<0.01	<0.01	0.01	<0.01	<0.01	<0.01	<0.01	<0.01	<0.01	0.01
Cs <sub>2</sub> O	%	0.06	0.01	<0.01	<0.01	<0.01	<0.01	0.01	<0.01	0.01	<0.01
Rb <sub>2</sub> O	%	0.23	0.11	0.13	0.09	0.21	0.10	0.21	0.15	0.25	0.13
Li <sub>2</sub> O	%	0.48	0.23	0.26	0.09	0.16	0.19	0.24	0.18	0.18	0.32
Na <sub>2</sub> O	%	0.09	0.58	0.71	0.68	0.68	0.76	0.43	0.63	0.51	0.43
K <sub>2</sub> O	%	9.41	10.35	10.50	10.95	10.51	10.77	10.85	10.61	10.79	10.29
F	%	2.17	0.92	2.03	1.14	1.44	1.55	1.14	1.48	1.45	1.41
F <sub>ekv</sub>	%	−0.92	−0.39	−0.85	−0.48	−0.61	−0.65	−0.48	−0.62	−0.61	−0.60
<b>Total</b>	%	96.18	96.07	96.97	95.91	96.74	97.16	96.03	96.03	96.34	96.35
Si	apfu	5.583	6.152	6.293	6.312	6.270	6.266	6.275	6.256	6.337	6.264
Ti	apfu	0.299	0.038	0.049	0.040	0.004	0.024	0.010	0.007	0.006	0.016
Al	apfu	3.482	5.408	5.079	5.159	5.267	5.303	5.250	5.298	5.148	5.218
Fe	apfu	2.898	0.288	0.457	0.333	0.483	0.267	0.458	0.452	0.499	0.438
Mn	apfu	0.069	0.008	0.009	0.006	0.009	0.005	0.009	0.008	0.011	0.008
Mg	apfu	0.918	0.185	0.159	0.155	0.019	0.125	0.020	0.009	0.020	0.132
Zn	apfu	0.020	0.003	0.005	0.004	0.003	0.003	0.006	0.005	0.005	0.004
Ca	apfu	0.000	0.000	0.001	0.000	0.000	0.000	0.000	0.000	0.000	0.001
Cs	apfu	0.004	0.000	0.000	0.000	0.000	0.000	0.000	0.000	0.001	0.000
Rb	apfu	0.015	0.006	0.007	0.005	0.012	0.006	0.012	0.009	0.014	0.008
Li	apfu	0.302	0.123	0.140	0.048	0.084	0.104	0.129	0.098	0.098	0.175
Na	apfu	0.028	0.149	0.184	0.178	0.176	0.197	0.112	0.166	0.134	0.112
K	apfu	1.860	1.767	1.803	1.885	1.804	1.824	1.873	1.834	1.863	1.764
F	apfu	1.066	0.389	0.862	0.486	0.611	0.651	0.487	0.634	0.620	0.601
Li	ppm	2253	1065	1201	412	721	904	1103	835	840	1505
Sc	ppm	25.1	30.7	90.5	14.4	1.8	26.6	1.2	0.7	2.0	2.4
Ga	ppm	74	110	153	131	141	148	158	126	127	111
Ge	ppm	4.0	4.0	4.2	4.2	7.1	4.2	8.1	6.3	6.9	6.0
Rb	ppm	1960	1694	1936	1698	2541	1984	3264	2416	2549	2731
Nb	ppm	89	74	100	55	183	109	196	124	136	52
In	ppm	0.41	0.93	1.19	0.93	1.42	0.70	1.37	0.95	1.18	1.17
Sn	ppm	73	100	91	115	143	66	177	126	420	335
Cs	ppm	310	41	42	56	111	34	157	89	126	147
Ta	ppm	5.8	9.1	12	10	63	20	38	24	56	17
W	ppm	6.1	64	83	71	99	83	114	91	98	88
Tl	ppm	11.9	6.2	7.2	8.4	9.8	7.2	15.6	10.1	11.0	12.6

Both micas are enriched in Sn, W, Nb, and Ta (Figure 8e–h), but the behavior of these elements is, upon closer inspection, different. While biotite from porphyritic granite contains 70–80 ppm Sn, associated muscovite is enriched up to 350 ppm Sn, Sn being well positively correlated with Li. Even higher Sn contents were found in muscovite from greisenized granite and veins (200–400 ppm Sn) and especially in muscovite from micaceous greisen (420–630 ppm Sn), although with no correlation to Li. Mica grains, which are the richest in tin, are the poorest in Na and Ti in the whole dataset.

The contents of W in biotite and associated primary Li-enriched muscovite in porphyritic granite are lower than 40 ppm, while Li-poor muscovite grains in altered porphyritic granite and muscovite grains from leucogranite, greisen, and quartz veins are enriched to 40–140 ppm W.

Biotite usually contains 40–50 ppm Nb, similar to muscovite from porphyritic granite and quartz veins (5–100 ppm Nb), while muscovite grains from leucogranite and greisen are enriched in Nb (50–250 ppm Nb). Tantalum shows a similar distribution: relatively low Ta contents were found in biotite and muscovite from porphyritic granite

(mostly < 20 ppm Ta) and quartz veins (<30 ppm Ta), while an enrichment of up to 125 ppm Ta was found in leucogranite and greisen. The Nb/Ta value in micas from the porphyritic granite varies only slightly around Nb/Ta = 10, which is substantially higher than the bulk-rock value of 2.9–4.6. This supports the experimental results of Stepanov et al. [37] that the  $K_d^{mica/melt}$  is higher for Nb than for Ta; in this case, Ta is preferentially accommodated in rutile. In leucogranites and greisenized granites/greisen, the mica Nb/Ta values are widely scattered and reduced to 1–2 due to a Ta enrichment, which is consistent with bulk values in these rock types. When Ti minerals disappear from rocks re-equilibrated with fluids, Ta becomes relatively enriched in mica.

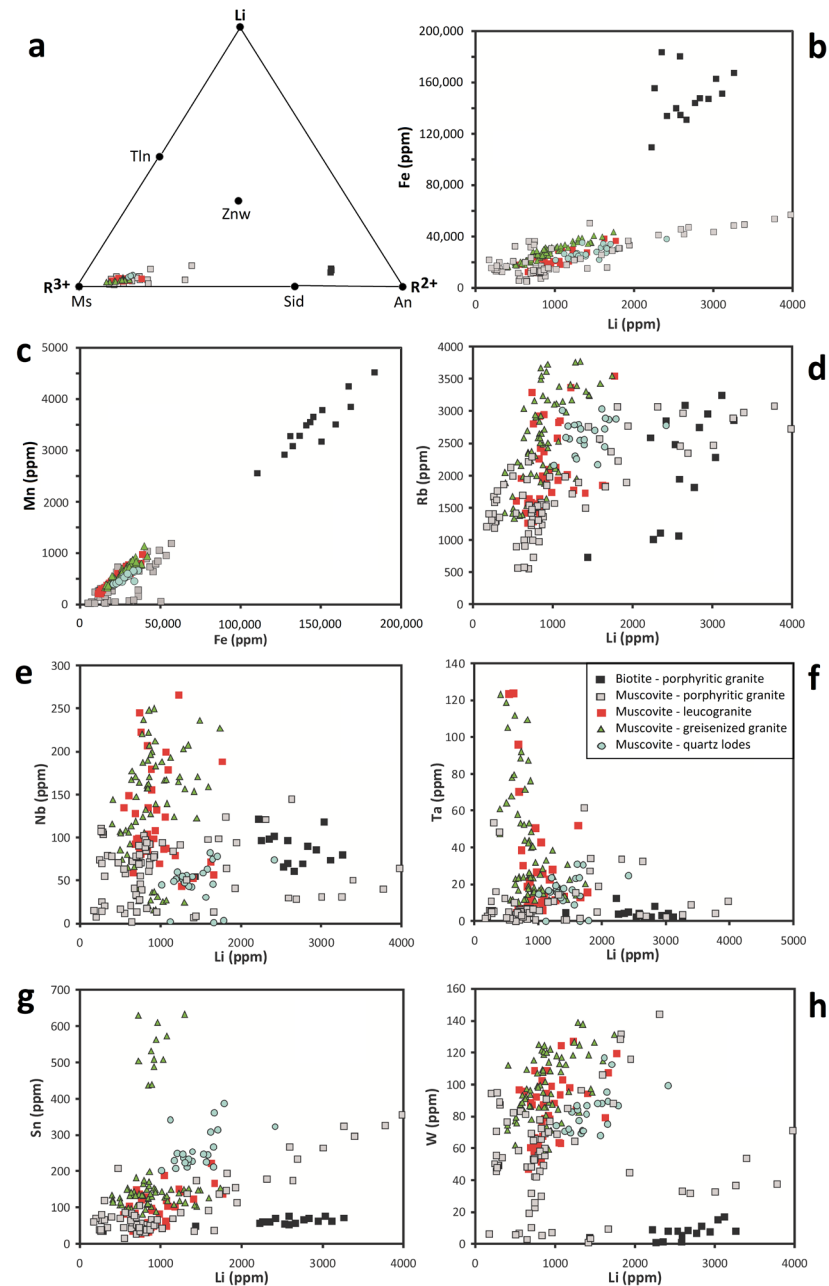


**Figure 8.** The classification and contents of minor and trace elements in micas: (a) classification diagram of Li-micas according to Foster [38]; (b) Li vs. Fe; (c) Fe vs. Mn; (d) Li vs. Rb; (e) Li vs. Nb; (f) Li vs. Ta; (g) Li vs. Sn; (h) Li vs. W. Means of samples are shown in Figure a (combination of EMP and LA data) while individual LA spots are shown in other figures.

#### 4.5. Feldspars

About 70 EMPA of feldspar were made; typical compositions are shown in Table 5. After quartz, feldspars are the most abundant minerals in granites from Panasqueira in amounts of 29–38 vol.% albite and 12–13 vol.% K-feldspar (Table 1). In greisen, only relicts armored in quartz (<1 vol.%) have been preserved. Feldspars in the Panasqueira granites are nearly pure albite with max. 1% of Kfs component and max. 2% of anorthite component, while the K-feldspar contains max. 2% of albite component. As is usual in peraluminous rocks, feldspars are enriched in phosphorus [39] (Table 5): about 0.2 wt.% P<sub>2</sub>O<sub>5</sub> are common in both feldspars; some Kfs grains from leucogranite and albite inclusions armored in quartz crystals from greisenized granite are enriched up to 0.8–1.2 wt.% P<sub>2</sub>O<sub>5</sub> (0.45 apfu P) (Figure 9). The only other minor element present in K-feldspar is rubidium in amounts of 0.1–0.2 wt.% Rb<sub>2</sub>O (max. 0.004 apfu Rb) with no statistical difference between the porphyritic and leucocratic granites.

**Table 5.** Chemical composition (wt.%, EMPA) and empirical formulae of feldspar.

Mineral		K-Feldspar						Plagioclase					
Sample		5	28	8	37	9	11	5	28	8	37	9	10
Rock		Porphyritic Granite		Leucogranite		Greisenized Granite		Porphyritic Granite		Leucogranite		Greisenized Granite	
Spot		7	21	25	50	38	68	9	24	32	48	41	58
P <sub>2</sub> O <sub>5</sub>	wt.%	0.26	0.14	0.11	0.97	0.12	0.82	0.15	0.15	0.09	0.18	0.13	1.11
SiO <sub>2</sub>	wt.%	64.23	64.23	63.90	63.73	64.59	63.53	68.71	68.04	68.49	68.38	68.44	66.41
Al <sub>2</sub> O <sub>3</sub>	wt.%	18.04	17.95	17.94	18.70	18.27	18.57	19.24	19.37	19.25	19.02	19.20	20.01
FeO	wt.%	<0.01	<0.01	0.02	0.01	<0.01	0.01	0.01	<0.01	<0.01	<0.01	0.01	0.01
CaO	wt.%	<0.01	<0.01	<0.01	0.01	<0.01	<0.01	0.04	0.07	0.03	0.02	<0.01	0.23
Rb <sub>2</sub> O	wt.%	0.14	0.20	0.10	0.20	0.13	0.14	<0.01	<0.01	<0.01	<0.01	0.02	<0.01
K <sub>2</sub> O	wt.%	17.03	16.33	17.19	15.95	16.52	16.64	0.07	0.15	0.16	0.16	0.16	0.16
Na <sub>2</sub> O	wt.%	0.29	0.26	0.22	0.56	0.23	0.43	11.85	11.70	11.65	11.48	11.62	11.56
<b>Total</b>	wt.%	100.00	99.11	99.48	100.13	99.86	100.13	100.06	99.48	99.67	99.24	99.57	99.50
P	apfu	0.010	0.006	0.004	0.038	0.005	0.032	0.005	0.006	0.003	0.007	0.005	0.041
Si	apfu	2.986	3.001	2.990	2.941	2.995	2.943	2.998	2.988	3.000	3.005	3.001	2.917
Al	apfu	0.988	0.989	0.989	1.017	0.998	1.014	0.989	1.003	0.994	0.985	0.992	1.036
Fe	apfu	0.000	0.000	0.001	0.000	0.000	0.000	0.000	0.000	0.000	0.000	0.000	0.000
Ca	apfu	0.000	0.000	0.000	0.001	0.000	0.000	0.002	0.003	0.001	0.001	0.000	0.011
Rb	apfu	0.003	0.004	0.002	0.004	0.003	0.003	0.000	0.000	0.000	0.000	0.000	0.000
K	apfu	1.010	0.973	1.026	0.939	0.977	0.983	0.004	0.008	0.009	0.009	0.009	0.009
Na	apfu	0.026	0.023	0.020	0.050	0.021	0.038	1.003	0.996	0.989	0.978	0.988	0.984

The contents of P in feldspars are a function of bulk-rock P contents and peraluminosity of the melt (ASI):  $DP^{Afs/melt} = 2.05 \times ASI - 1.75$  [39]. During postmagmatic hydrothermal processes, the contents of P in feldspars decrease [40]. At Panasqueira, ASI equals 1.4 in porphyritic granite, while ASI = 1.2–1.5 was found in leucogranite; the relation between P contents in bulk rock and feldspars is shown in Figure 9. Analyses lying within the expected correlation zone between the bulk and feldspar P contents represent the primary magmatic composition of feldspars, while points lying distinctly below this zone indicate a different degree of hydrothermal alteration. (Two analyses positioned well above the correlation line for ASI = 1.5 are probably products of accidental hits of micro inclusions of some phosphate.)

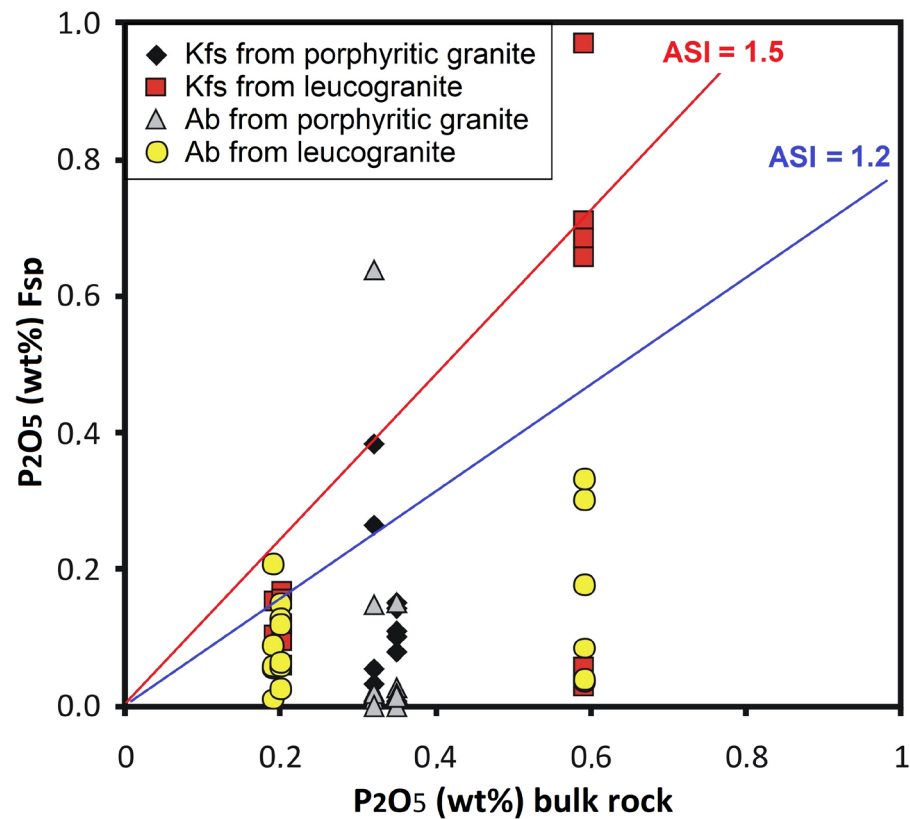


Figure 9. The contents of phosphorus in alkali feldspars. The contents of P<sub>2</sub>O<sub>5</sub> in magmatic feldspar are a function of bulk P contents and the peraluminosity of the melt [39].

4.6. Apatite

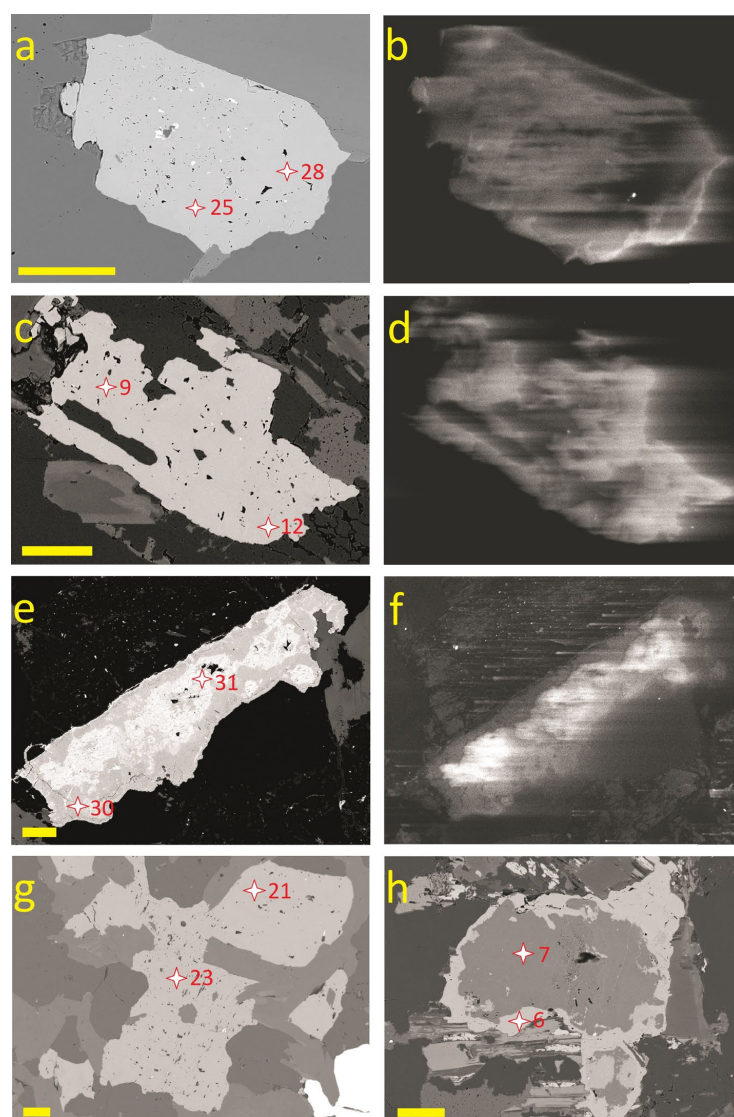
Apatite is a ubiquitous accessory mineral at Panasqueira, the most common among all phosphates. It forms mostly roughly isometric anhedral grains, scarcely subhedral columnar grains, 0.5–1 mm in size (Figure 10). Apatite emitted strong but in detail variable CL in most cases. The intensity of CL sometimes corresponds to the brightness of the BSE image (Figure 10e vs. Figure 10f), but the BSE image is usually homogeneous also in strongly CL-variable grains (Figure 10c vs. Figure 10d).

Table 6. Chemical composition (wt.%, EMPA) and empirical formulae of apatite. All Ce-values below detection limit (bdl) of 0.03 wt.% Ce<sub>2</sub>O<sub>3</sub>.

Rock	Porphyritic Granite				Leucogranite			Greisen		Porphyrit. Granite	Detection Limit
Sample	5	5	28	8	8	37	37	9	10	5	
Spot	6	25	16	9	12	30	31	13	23	7	
Mineral	Ap	Ap	Ap	Ap	Ap	Ap	Ap	Ap	Ap	Isokite	
P <sub>2</sub> O <sub>5</sub>	43.33	43.95	42.15	43.10	43.42	40.52	43.33	43.03	42.89	39.53	0.02
SiO <sub>2</sub>	0.01	0.06	na	bdl	0.01	bdl	bdl	na	bdl	0.03	0.01
SO <sub>3</sub>	0.02	0.01	na	bdl	0.01	1.47	0.02	na	0.01	1.65	0.01
CaO	51.43	53.51	50.98	51.03	50.92	52.46	45.78	52.32	50.34	29.64	0.02
MnO	2.62	0.27	2.83	2.78	2.96	0.23	7.24	2.67	3.55	0.05	0.02
FeO	1.00	0.02	0.30	0.13	1.07	0.29	0.86	0.22	0.21	0.24	0.02
SrO	bdl	0.10	0.96	0.38	bdl	0.03	0.21	0.75	0.38	bdl	0.03
MgO	0.04	bdl	bdl	bdl	0.02	0.06	bdl	0.01	0.01	22.52	0.01
Na <sub>2</sub> O	0.01	0.06	na	0.01	0.01	0.56	0.04	na	0.02	0.71	0.01
F	3.40	4.17	4.47	3.41	3.26	3.56	3.03	4.57	3.40	9.10	0.03
F eq.	−1.43	−1.76	−1.88	−1.44	−1.38	−1.50	−1.28	−1.93	−1.43	−3.84	
Total	100.42	100.40	99.81	99.40	100.31	97.67	99.24	101.65	99.37	99.65	

Table 6. Cont.

Rock	Porphyritic Granite		Leucogranite		Greisen		Porphyrit. Granite	Detection Limit		
P	3.057	3.083	3.034	3.070	3.064	2.930	3.102	3.035	3.063	0.980
Si	0.001	0.005		0.001	0.001					0.001
S	0.001	0.001		0.001	0.001	0.094	0.002		0.000	0.036
Ca	4.592	4.750	4.643	4.599	4.548	4.800	4.147	4.670	4.550	0.930
Mn	0.185	0.019	0.204	0.198	0.209	0.016	0.519	0.188	0.254	0.001
Fe	0.070	0.002	0.021	0.009	0.075	0.021	0.061	0.016	0.015	0.006
Sr		0.005	0.047	0.018		0.001	0.010	0.036	0.019	
Mg	0.004		0.001		0.002	0.008		0.001	0.001	0.983
Na	0.002	0.010		0.001	0.001	0.093	0.006		0.003	0.040
F	0.896	1.093	1.200	0.907	0.859	0.962	0.810	1.200	0.907	0.843



**Figure 10.** Back-scattered electron images (BSE) and CL images (CL) of typical apatite grains with locations of EMP analyses: (a,b) BSE and CL images of an apatite grain from porphyritic granite (#5); (c,d) BSE and CL images of an apatite grain from leucocratic granite (#8); (e,f) BSE and CL images of an apatite grain from leucogranite (#37), note the strong zoning in both images: core of the grain is enriched especially in Mn; (g) apatite grains from greisen (#10); (h) a zoned phosphate grain: apatite core is rimmed by isokite (porphyritic granite, #5). Scale bars are 100  $\mu\text{m}$  in all cases. Stars indicate localization of EMP analyses, compare Table 6.

Seventy EMP analyses of typical apatite were performed from all rock types (Table 6, Figure 11). All analyses correspond to fluorapatite with mostly 0.9–1 F apfu. The most common minor element is Mn (commonly 0–4 wt.%, max. 7.5 wt.% MnO) which prevails over Fe (0–1.1, max. 2.3 wt.% FeO). The contents of Sr are mostly lower than 0.2 wt.% SrO, but individual grains containing 0.7–0.95 wt.% SrO were found in all rock types, showing a negative correlation with Fe (Figure 11a). Among other elements, the contents of SiO<sub>2</sub>, SO<sub>3</sub>, and Na<sub>2</sub>O are lower than 0.1 wt.%, and the content of Ce is lower than the detection limit in all cases.

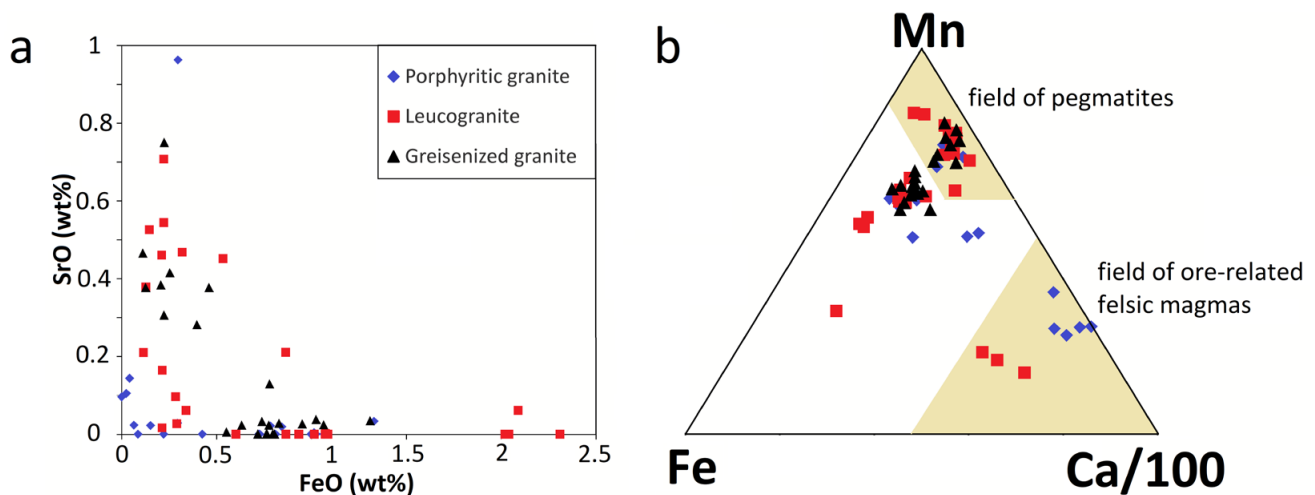


**Figure 11.** Chemical composition of apatite: (a) FeO vs. SrO; (b) a ternary diagram Ca/100–Mn–Fe (atomic proportions) according to [41].

Relations among Ca, Mn, and Fe vary strongly (Figure 11b), but the Mn/Fe ratios are substantially higher than unity in most cases. Fe contents are negatively correlated, while Sr contents are positively correlated with the intensity of CL. The chemical composition of apatite was probably influenced by late fluids sourced in the surrounding schists.

Besides apatite, granites from Panasqueira locally contain phosphates of Mg, Ca, Mn, and Fe. Among them, isokite, ideally CaMg(PO<sub>4</sub>)F, was identified, probably forming late hydrothermal rims around apatite grains in porphyritic granite (Figure 10h, Table 6).

#### 4.7. Zircon

In porphyritic granite, zircon commonly forms euhedral, short columnar crystals max. 60 × 30 μm in size, and rarely occurs as needle-like crystals max. 150 μm long, some of them regularly zoned in BSE. The relatively BSE-lighter zones were found to be enriched in Hf and U. In leucogranite, zircon forms euhedral crystals (10–40 μm across), oscillatory-zoned and associated with monazite and uraninite, although smaller mottled (<20 μm) grains are more common (Figure 12).

**Table 7.** Chemical composition (wt.%, EMPA) and empirical formulae of zircon, bdl = below detection limit.

Sample	5			28			47			53			37	
Localization	Borehole 18D			Borehole 34E			Cupola			Cupola			Borehole 3G	
Rock Type	Porphyritic Granite			Porphyritic Granite			Leucogranite			Leucogranite			Leucogranite. Greisenized	
Spot	20	21	19	4	5	11	20	21	27	28	29	30	9	10
P <sub>2</sub> O <sub>5</sub>	0.17	0.06	0.15	1.45	1.03	0.76	0.27	0.48	0.13	2.32	0.97	0.38	0.45	0.39
As <sub>2</sub> O <sub>3</sub>	bdl	bdl	bdl	bdl	bdl	bdl	bdl	bdl	bdl	bdl	bdl	bdl	bdl	0.01
SiO <sub>2</sub>	32.98	33.39	31.66	31.39	31.68	29.03	31.57	32.04	33.21	29.27	30.78	32.40	29.88	30.75
ZrO <sub>2</sub>	64.23	64.97	67.14	61.99	63.95	58.33	57.77	59.73	62.88	55.58	58.55	59.26	55.76	53.84
HfO <sub>2</sub>	2.02	1.87	1.63	1.49	1.30	3.23	4.76	3.21	1.93	3.28	2.56	4.87	3.45	4.71
ThO <sub>2</sub>	0.05	0.04	bdl	0.05	0.09	0.13	0.03	0.09	0.03	0.06	0.06	bdl	0.18	0.04
UO <sub>2</sub>	0.32	0.10	0.05	0.21	0.12	3.25	0.83	0.81	0.06	2.24	1.75	0.91	2.49	3.83
Y <sub>2</sub> O <sub>3</sub>	0.14	0.05	0.10	1.64	1.23	0.67	0.07	0.23	0.21	1.59	0.54	0.26	0.26	0.21
Yb <sub>2</sub> O <sub>3</sub>	0.04	bdl	0.03	0.41	0.29	0.27	0.11	0.20	bdl	0.59	0.22	0.23	0.15	0.17
Al <sub>2</sub> O <sub>3</sub>	0.00	0.04	bdl	bdl	0.02	0.29	0.03	0.05	bdl	bdl	bdl	bdl	0.22	0.33
Sc <sub>2</sub> O <sub>3</sub>	0.02	0.05	bdl	0.08	0.07	0.21	0.16	0.12	0.07	0.71	0.37	0.07	0.12	0.09
MnO	bdl	0.05	0.02	bdl	bdl	0.00	0.05	0.04	bdl	bdl	bdl	0.06	0.03	0.04
FeO	0.37	0.24	0.35	0.30	0.28	0.08	0.31	0.06	0.06	0.31	0.24	0.13	0.37	0.44
CaO	0.01	0.01	bdl	0.03	0.01	0.03	0.19	0.29	0.04	bdl	0.01	0.03	0.32	0.43
<b>Total</b>	100.34	100.84	101.14	99.02	100.06	96.26	96.12	97.34	98.62	95.96	96.05	98.61	93.67	95.29
<b>P</b>	0.004	0.001	0.004	0.038	0.027	0.021	0.007	0.013	0.003	0.064	0.026	0.010	0.013	0.011
<b>As</b>	0.000	0.000	0.000	0.000	0.000	0.000	0.000	0.000	0.000	0.000	0.000	0.000	0.000	0.000
<b>Si</b>	1.009	1.013	0.970	0.972	0.973	0.956	1.018	1.013	1.026	0.950	0.991	1.019	0.998	1.016
<b>Zr</b>	0.958	0.961	1.004	0.936	0.958	0.937	0.909	0.921	0.947	0.879	0.920	0.909	0.908	0.867
<b>Hf</b>	0.018	0.016	0.014	0.013	0.011	0.030	0.044	0.029	0.017	0.030	0.023	0.044	0.033	0.044
<b>Th</b>	0.000	0.000	0.000	0.000	0.001	0.001	0.000	0.001	0.000	0.000	0.000	0.000	0.001	0.000
<b>U</b>	0.002	0.001	0.000	0.001	0.001	0.024	0.006	0.006	0.000	0.016	0.013	0.006	0.019	0.028
<b>Y</b>	0.002	0.001	0.002	0.027	0.020	0.012	0.001	0.004	0.003	0.027	0.009	0.004	0.005	0.004
<b>Yb</b>	0.000	0.000	0.000	0.004	0.003	0.003	0.001	0.002	0.000	0.006	0.002	0.002	0.002	0.002
<b>Al</b>	0.000	0.001	0.000	0.000	0.001	0.011	0.001	0.002	0.000	0.000	0.000	0.000	0.009	0.013
<b>Sc</b>	0.001	0.001	0.000	0.002	0.002	0.006	0.004	0.003	0.002	0.020	0.010	0.002	0.003	0.003
<b>Mn</b>	0.000	0.001	0.000	0.000	0.000	0.000	0.001	0.001	0.000	0.000	0.000	0.002	0.001	0.001
<b>Fe</b>	0.009	0.006	0.009	0.008	0.007	0.002	0.008	0.002	0.002	0.008	0.006	0.003	0.010	0.012
<b>Ca</b>	0.000	0.000	0.000	0.001	0.000	0.001	0.006	0.010	0.001	0.000	0.000	0.001	0.011	0.015
<b>Zr/Hf</b>	54.4	59.4	70.4	71.1	84.0	30.8	20.8	31.8	55.8	28.9	39.1	20.8	27.6	19.5

Eighty EMP analyses of zircon were performed; typical compositions are given in Table 7. Besides silicon and zirconium, hafnium is the most common element: mostly 1.2–2.0 wt.% HfO<sub>2</sub> was measured in zircon from porphyritic granite and 3.5–6.5 wt.% HfO<sub>2</sub> in zircon from leucogranite. The corresponding atomic Zr/Hf values are mostly 40–90 and 15–30, respectively. The contents of radioactive elements U and Th are highly variable, reaching max. 3.8 wt.% UO<sub>2</sub> and 0.8 wt.% ThO<sub>2</sub> (Figure 13a). The contents of Y and HREE vary across broad intervals, mostly lying within 0.2–1.5 wt.% Y<sub>2</sub>O<sub>3</sub> (Figure 13b) and 0.1–0.4 wt.% Yb<sub>2</sub>O<sub>3</sub>. The contents of scandium are usually <0.1 wt.% Sc<sub>2</sub>O<sub>3</sub>, higher values up to 0.7 wt.% Sc<sub>2</sub>O<sub>5</sub> are scarce, with no relation to a specific rock type.

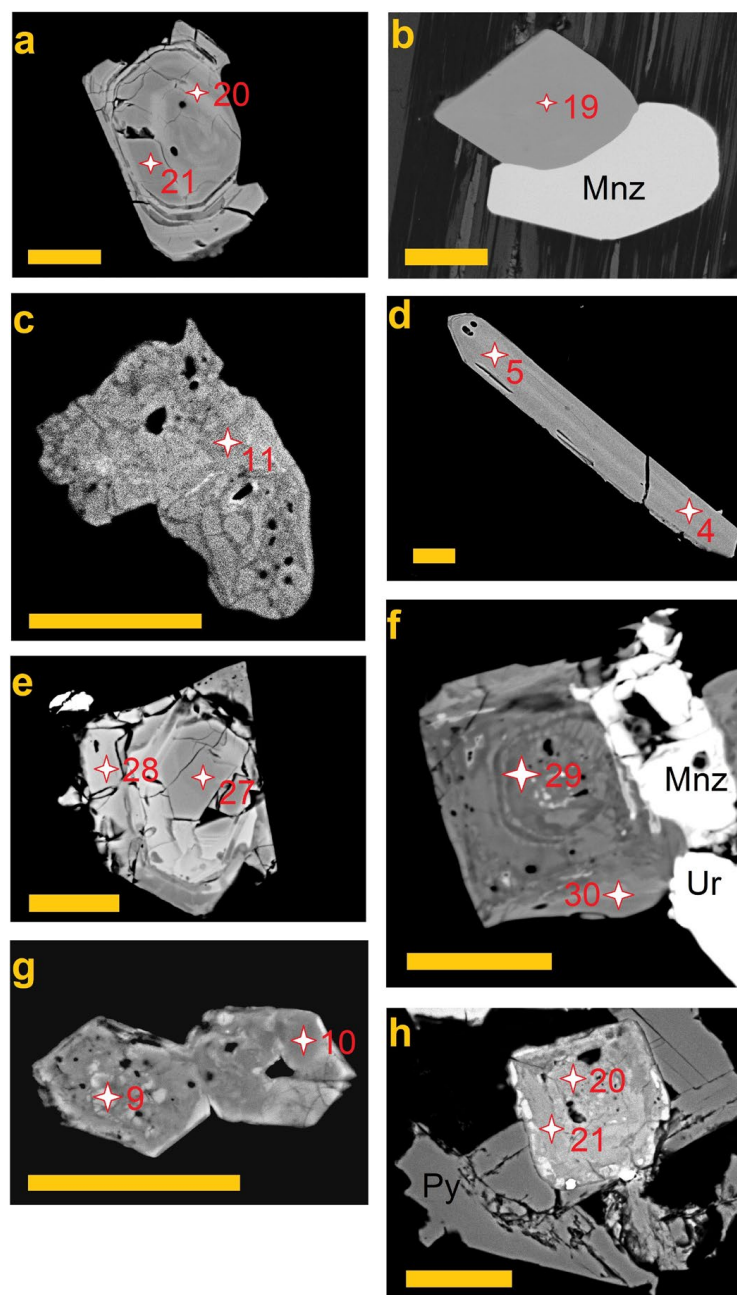


**Figure 12.** Back-scattered electron images (BSE) of typical zircon crystals with locations of EMP analyses: (a) a zoned crystal from porphyritic granite (#5); (b) a homogeneous zircon grain (dark gray) at contact with monazite (light), porphyritic granite (#5); (c) a strongly altered grain, porphyritic granite (#28); (d) a needle-like crystal, porphyritic granite (#28); (e) a cracked zoned crystal with a Hf-enriched rim, leucogranite (#53); (f) a zoned zircon crystal with a Hf-enriched rim (gray) associated with monazite and uraninite (bright), leucogranite (#53); (g) two small crystals with  $\mu\text{m}$ -sized uraninite admixtures, leucogranite (#37); (h,a) zoned crystal with a lighter core, a darker mantle and a bright rim associated with pyrite (dark gray), leucogranite (#47). Scale bars 20  $\mu\text{m}$  in all cases. Stars indicate localization of EMP analyzes, compare Table 7. Mnz—monazite, Ur—uraninite, see Table 7.

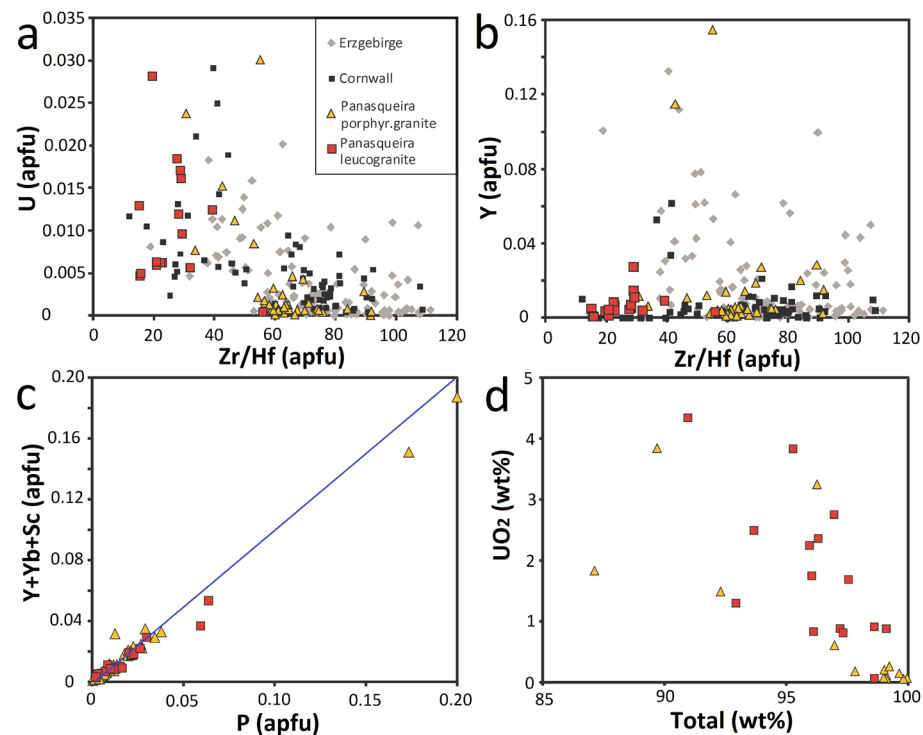


**Figure 13.** Chemical composition of zircon: (a) Zr/Hf vs. U; (b) Zr/Hf vs. Y; (c) P vs. Y; (d) total vs. UO<sub>2</sub>. For comparison, data of zircons from peraluminous rare-metal granites from the Erzgebirge [42] and Cornwall [43] are shown in (a,b).

The contents of P are usually lower than 1 wt.% P<sub>2</sub>O<sub>5</sub>, rarely reaching 6 wt.% P<sub>2</sub>O<sub>5</sub>, correlating well with the sum of trivalent elements forming the xenotime–pretilite component isostructural with zircon:  $Zr^{4+} + Si^{4+} \leftrightarrow (Y, Yb, Sc)^{3+} + P^{5+}$  (Figure 13c). Many zircon grains are metamictized due to the high U contents, i.e., their structure is destroyed and partly diluted. This is well documented by the negative correlation between the contents of UO<sub>2</sub> and analytical totals of EMP analyses (Figure 13d).

## 5. Discussion

### 5.1. Evolution of the Panasqueira Hidden Pluton

Most granites within the Panasqueira pluton are influenced by post-magmatic alteration. The intensity of this alteration increases upwards and towards the center, culminating with total greisenization of the hidden cupola. Primary feldspars and micas were modified in their composition. A correct interpretation of the inner structure of the pluton, including its original chemical and mineral composition, is problematic. Even so, the compositions of minerals relatively resistant to hydrothermal reactions, such as quartz and zircon, can provide some clues.

Quartz from porphyritic granite and leucogranite can be clearly discriminated based on the contents of Ti, Fe, and Ge, the former being richer in Ti (40–170 vs. mostly 10–30 ppm) and Fe (3–70 vs. <5 ppm), but poorer in Ge (0.5–1.5 vs. mostly 1–3). Similarly, zircon from the two granite types differs in the shape of grains and especially in the degree of Hf enrichment: Zr/Hf values are 40–90 in porphyritic granite vs. 15–30 in leucogranite. These are strong arguments for the existence of two comagmatic successive intrusion units differing in the degree of magmatic fractionation [23,32,35,37,44,45].

The extent of the whole pluton is roughly delineated by the gravity survey [27]. The upper contact of the major part of the pluton lies at a level of 0–200 m above sea level. Local elevations of the upper granite contact were already found: the hidden Panasqueira cupola, occasionally found by mining works; and the hidden elevation at Rio reached by three boreholes (12C, 19F, 20F). Arching of the upper contact of the rare-metal granite (RMG)

plutons with the formation of cupolas or steep stocks is generally an important supporting factor for the localization of fluid flow and the origin of mineralization [18,20,46].

The pluton elevation at Rio is small in area and relatively flat, rising above its surroundings by ca. 200 m. Two-mica porphyritic granite from borehole 20F is lined by a thin zone of stockscheider, locally greisenized and mineralized by disseminated sulfides. No wolframite or cassiterite was found, but rare quartz–wolframite veinlets hosted by the schists were mined at Rio in the past. This indicates that the relatively less fractionated porphyritic granite was able to produce small volumes of ore-productive fluids.

The areal extent of the pluton elevation between Barroca Grande and Panasqueira villages indicated by gravity survey [27] and boreholes is ca. 6 km<sup>2</sup> at the level of 400 m above sea level (Figure 1). This elevation passes to a steep stock, traditionally termed as “cupola”, reaching the level of ca. 650 m a.s.l. A detailed examination of borehole cores proved a more complicated shape of the cupola than previously published (compare Figures 2 and 14), with several generally flat apophyses. In this cupola, porphyritic granite was found only in two boreholes (18D, 34E) on its eastern slope near the level of 400 m a.s.l., with mild greisenization in borehole 18D. Recently, a new borehole SCB2 in this area led to different geological interpretations [17,20]. The rest of the cupola is formed exclusively by leucogranite, strongly greisenized above the level of 530 m a.s.l. The greisen passes upwards to a body that is composed almost exclusively of quartz, 25 m thick (“quartz cap”). This part of the cupola has been, unfortunately, inaccessible for a long time, and no relevant samples exist. Kelly and Rye [4] stressed the apparent continual transition of the quartz cap into flat quartz–wolframite lodes, although the cap itself was not mineralized. Whereas greisen represents the metasomatized upper part of the granite, the quartz cap most probably represents the hydrothermal filling of the space opened between the greisenized granite and the host schists due to the shrinkage of pluton upon its cooling. This shrinkage and the subsidence of the upper parts of the pluton resulted in the opening of flat joints within the overlying schists, which were filled with quartz veins ( $\pm$ Ms, Wlf, etc.) simultaneously with the formation of the quartz cap.

A recent geochemical study about Panasqueira granites by Marignac et al. [20] was based on only an 85 m long interval of borehole SCB2, including some samples from the cupola base. In the borehole profile, Marignac distinguished upper G1 porphyritic granite and lower G2 leucogranite, both intruded by thin aplite dikes (designated as G3) and locally slightly greisenized. The contact between G1 and G2 was interpreted as an intrusive one, accentuated by a thin stockscheider. This finding is in general agreement with our idea of two main intrusive units forming the pluton. Chemical data of [20] thus fit well with the present analytical results (Figure 5) if a ubiquitous postmagmatic alteration is considered.

Available bulk chemical data (Table 1, Figure 5) show a generally increasing degree of magmatic fractionation, i.e., a depletion in compatible elements (e.g., Fe, Zr, REE) and an enrichment in incompatible elements (e.g., Rb, Nb, Ta) from porphyritic granite to leucogranite. Among rare metals, a contrasting behavior is observed between Nb and Ta and between Sn and W. In this succession, the contents of Nb and Ta increase (from ~15 to 15–35 ppm Nb and from 5 to 10 to 10 to 20 ppm Ta), and their ratios slightly decrease (from mostly 2.5–4.5 to ~2), thereby following the expected fractional evolution [47]. The contents of Sn and W vary widely in both granites (30–80 ppm Sn, 10–28 ppm W) without a clear evolutionary trend; this possibly results from large-scale postmagmatic hydrothermal remobilization of Sn and W within the whole pluton, at least in the sampled areas.

Launay et al. [17] published geochemical data of quartz from the new borehole SCB2 on the NE slope of the granite cupola and from quartz from a gallery newly reaching the lower part of the cupola. Comparing these data with our dataset, a general agreement is found (Figure 15). The “granite” data by [17] agree well with the results of our analyses from the porphyritic granite, and their data from “greisenized granite + greisen” are compatible with our data from the leucogranite, indicating that a substantial portion of the quartz grains analyzed by [17] were relicts from the granitic stage. The “vein quartz” of [17] is often rich in Ti, which is unusual in common vein quartz [32]. Ti-rich

(10–20 ppm Ti) quartz samples represent rutile-rich selvages of quartz veins, and the high Ti mobility at this stage of vein evolution [13] is probably also responsible for the unusual Ti enrichment in hydrothermal quartz. No chemical data are available on quartz from the cap, but the compositional similarity between the greisen quartz and quartz from the ore veins may indicate that all these quartz varieties crystallized from identical or similar fluids. Nevertheless, the relative enrichment of rims of some granitic quartz crystals in Sn (Figure 7) documents the enrichment of tin in the residual portion of the magma already.

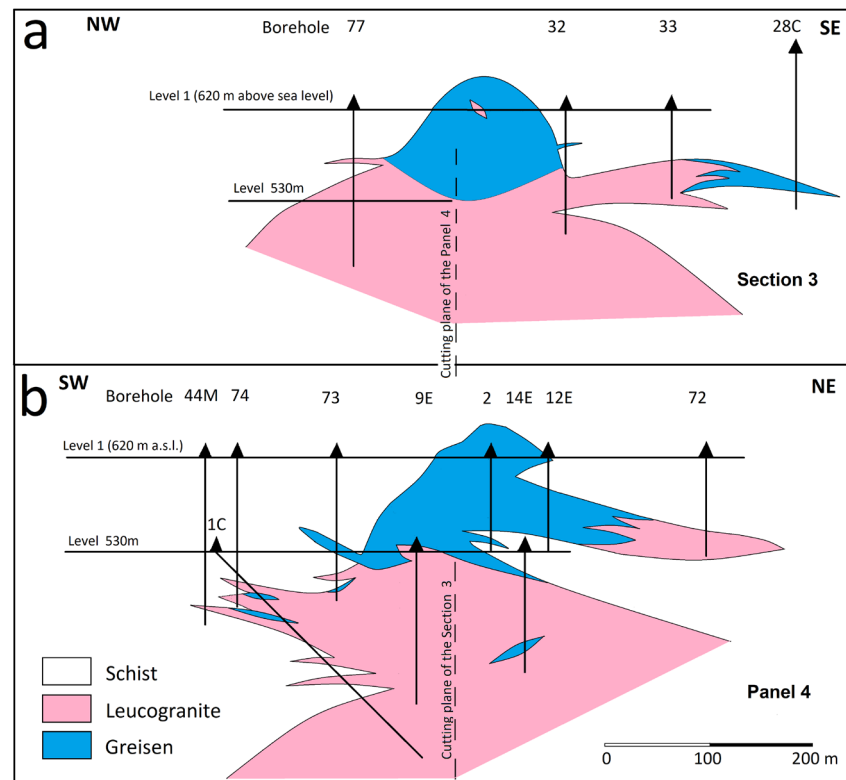


Figure 14. A cross-section through the Panasqueira hidden granite cupola according to re-evaluation of borehole cores: (a) NW–SE section along “Section 3”; (b) SW–NE section along “Panel 4”.

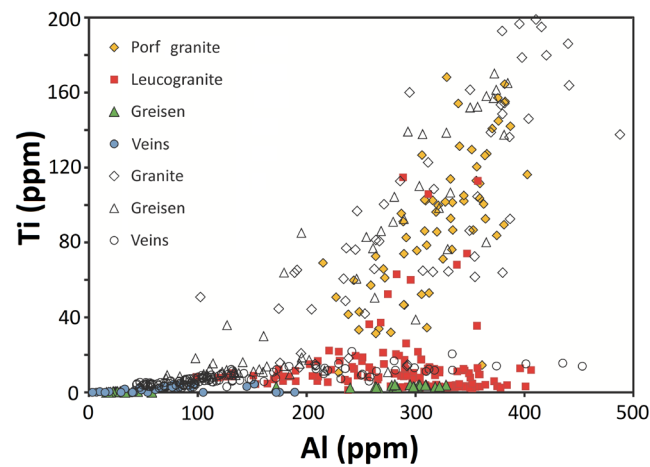
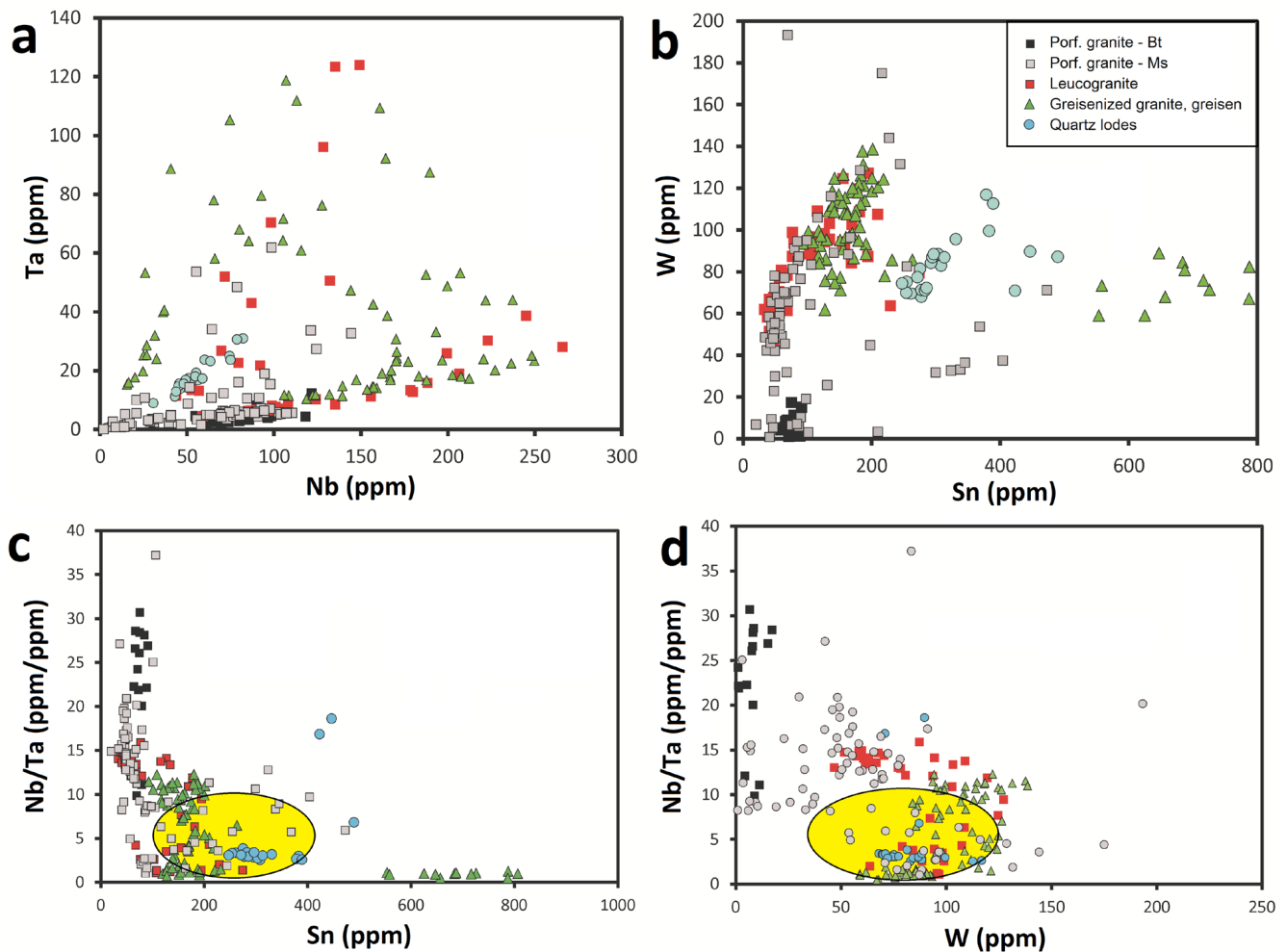


Figure 15. A comparison of our quartz data (colored symbols) with the data from borehole SCB2 and the new adit (B–W symbols) [17] in coordinates Al vs. Ti.

The composition of micas provides more straightforward information (Figure 16): most muscovite grains from leucogranite show approx. doubled Nb and Ta contents compared to muscovite from porphyritic granite, forming an array with Nb/Ta values of about 10, similar to those of relatively less fractionated parts of many RMG plutons worldwide [48]. This array (Figure 16a) is supposed to represent primary magmatic crystallization [36]. Some muscovite grains from leucogranite and most muscovite grains from greisen show a slight to strong Ta enrichment, with Nb/Ta values reaching 1. This should be attributed to a variable degree of hydrothermal re-equilibration.



**Figure 16.** Relations among HFSE metals in mica: (a) Nb vs. Ta; (b) Sn vs. W; (c) Nb/Ta vs. Sn; (d) Nb/Ta vs. W. Yellow fields indicate locations of the majority of greisen and vein micas analyzed by [14].

In contrast, muscovite in the quartz veins shows Nb/Ta values around 3, identical to most bulk-rock values in leucogranite, which probably represents the Nb/Ta value of the fluid. Generally lower contents of all metals in mica from the veins compared to those in mica from the greisen result from the incorporation of both elements into simultaneously formed wolframite.

Tin contents in granitic micas from Panasqueira, both muscovite and biotite, lying in the range of 50–200 ppm, are identical with Sn contents in micas from less fractionated RMGs worldwide. In contrast, tungsten contents in the range of 40–140 ppm are high compared to those in other Sn–W-mineralized plutons [48]. The majority of the analyzed mica grains form an array with a Sn/W ratio of about 3:2 (Figure 16b). This may represent primary magmatic growth, although some hydrothermal mobilization cannot be ruled out. A strong tin enrichment in sample #11 (mica-rich greisen, level 1, near the eastern contact of the cupola) may represent a local anomaly. Mica from the quartz veins is relatively Sn-enriched, while W was preferentially bound to simultaneously growing wolframite. The contents of both Sn and W in muscovite increase with decreasing Nb/Ta values (Figure 16c,d), corroborating an idea about a Sn,W,Ta-rich and Nb-impoorished character of hydrothermal fluids producing the Panasqueira mineralization.

Recently, [14] published trace element data of muscovite from the greisen and the veins; they reported Nb/Ta values of <2 in the greisen and 2–10 in the veins. The respective Sn contents are 100–300 ppm and 40–120 ppm, which is generally in good agreement with our data (Figure 16c,d).

### 5.2. Comparison with Peraluminous Granites from Cornwall, the Erzgebirge, and Other Areas

The granite pluton at Panasqueira is one of the numerous late Variscan peraluminous Sn ± W-bearing plutons cutting the Variscan orogen in western and central Europe. Many principal chemical similarities, as well as some interesting differences among typical peraluminous Sn–W granites from Cornwall, the Erzgebirge, Panasqueira, and neighboring Argemela, are shown in Figure 17. Among the compared granites, the Argemela stock [23,24,26,49] has an exceptional position in many features: it is the most fractionated in terms of K/Rb (10–20), Zr/Hf (2–6), and Nb/Ta (0.7–1.0) values, and simultaneously the most enriched in P, Rb, Cs, and Ta. On the other hand, Argemela granites are unusually poor in W and accompanied by a relatively very weak postmagmatic fluid activity. Excluding from further reasoning this unique magmatic system, all the other assessed plutons can be interpreted as having undergone a similar geochemical evolution, although values found at Panasqueira better correspond to medium-degree fractionated parts of other discussed plutons (Figure 17a,b) in terms of Zr/Hf, Nb/Ta, and K/Rb values.

Trends of the enrichment in F, P, Rb, Cs, Nb, Ta, W, and Sn in the Panasqueira pluton and in typical plutons from Cornwall and the Erzgebirge form mostly singular arrays. All rare-metal granites or, more correctly, granites spatially associated with Sn–W (Li, Nb, Ta) mineralizations, are enriched in volatiles (F, P, Figure 17c), rare alkalis (Rb, Cs, Figure 17d), and HFS ore elements (Nb, Ta, Sn, W, Figure 17e,f).

The Rb/Cs values for the Panasqueira granites vary between 18 and 32, being similar to the upper crust value of 20 [50]. This means that Rb and Cs have not fractionated from each other during the whole pluton evolution. An intensive Rb/Cs fractionation is typical for the strongly evolved late pluton members from Cornwall and the Erzgebirge and, of course, for the Argemela stock (Figure 17d). The Nb/Ta values for the Panasqueira porphyritic granite is 3–5, i.e., much lower than the upper crust value of 13. This indicates an already Ta-enriched source lithology, or productive fractionation in the lower, as yet not investigated part of the pluton.

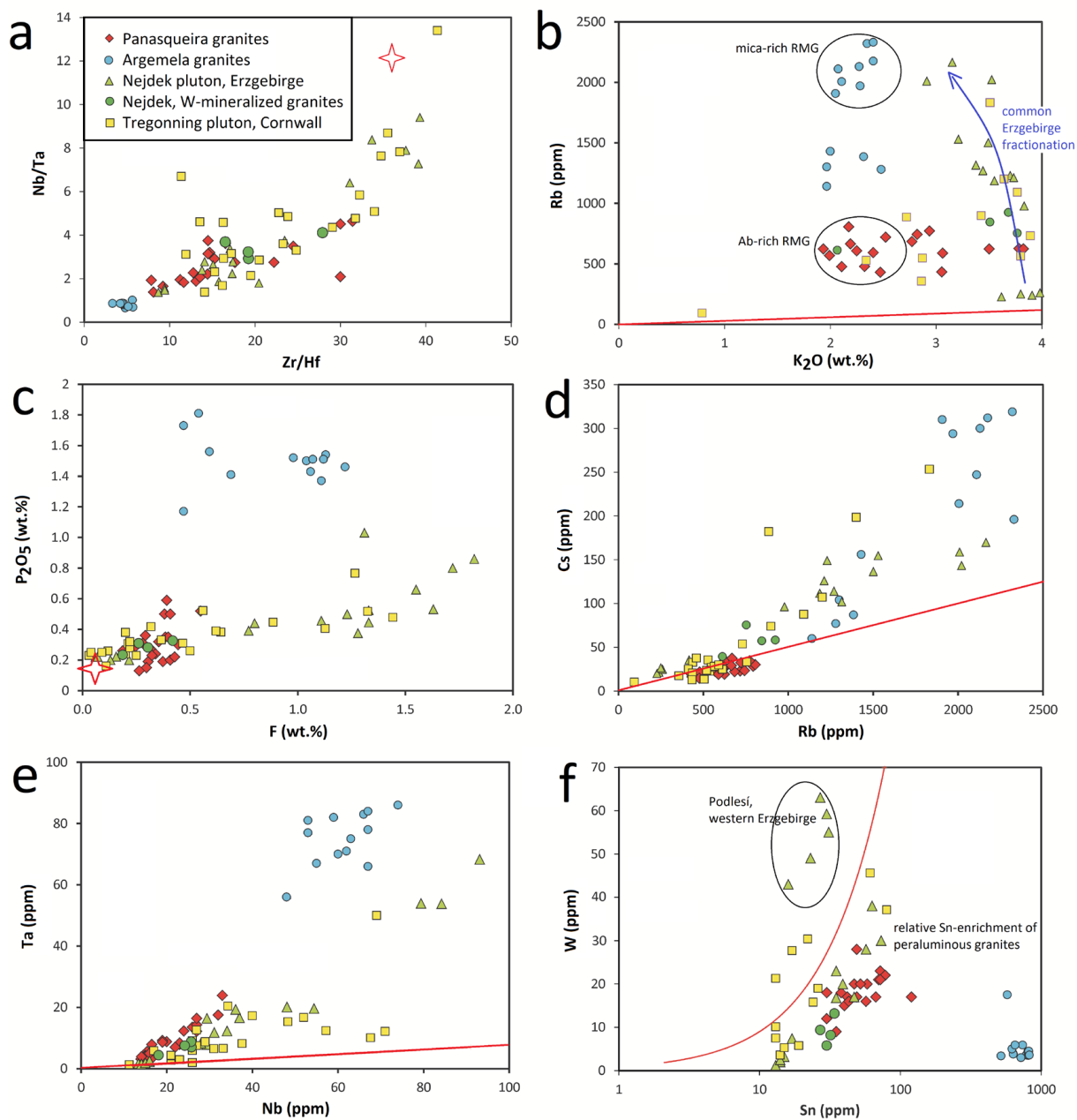


**Figure 17.** A comparison of bulk-rock contents of selected elements in European Variscan peraluminous granites: Panasqueira (this paper), Argemela [23], Land’s End pluton [51] and Tregoning pluton + Megilgar area [52] in Cornwall, and the Nejdek pluton [29] + associated W-producing subintrusions from the Erzgebirge (authors’ unpublished data): (a) Zr/Hf vs. Nb/Ta; (b) K vs. Rb; (c) P<sub>2</sub>O<sub>5</sub> vs. F; (d) Rb vs. Cs; (e) Nb vs. Ta; (f) Sn vs. W. Mean elemental ratios of the upper continental crust [50] are shown as a red line or an asterisk.

Tin and tungsten are enriched in porphyritic granite already, and this trend follows the common evolution of the majority of RMGs (Figure 17f). The relative enrichment in Sn relative to the upper crust W/Sn mean value (50) is caused by its more lithophilic character and is also common in specifically W-productive granites without or with very poor Sn mineralization, such as at Panasqueira and in granites with wolframite-bearing greisens in the western Erzgebirge [53]. In contrast, the Sn-productive Podlesi granite system in the western Erzgebirge shows strong W-enrichment in the late, yet completely magmatic (i.e., not metasomatized) facies [29]. The conspicuous difference in the behavior of Sn and W in the Panasqueira and Argemela magmatic systems, only 15 km apart, cannot be

explained by different source lithologies; the cause of this difference should be searched in the process of fractionation as an interesting topic for further research.

Igneous and hydrothermal quartz from Panasqueira can be compared with its equivalents from the Erzgebirge—see Figure 18a,b. During common magmatic fractionation of granites, Ti contents in quartz decrease along with stable or only slightly increasing Al [32,34,54]. In contrast, Al contents increase steeply in the late stages of extremely fractionated leucogranites, like at Podlesí [55] or Argemela [26]. In this comparison, granites from the Panasqueira pluton reached only an intermediate level of fractionation (Figure 18a). Hydrothermal quartz is usually relatively poorer in both these elements, which corresponds to the generally lower temperature of hydrothermal quartz from Sn–W greisens and veins [16,17,56,57]. Some of the analyses of greisen quartz from the Erzgebirge and Panasqueira show “granitic” composition; they actually stand for remnants of magmatic quartz (crystal cores), not reequilibrated during the greisenization. Certain differences in the contents of Ti between our data and the data of [17] (Figure 15) point to different degrees of hydrothermal equilibration in particular parts of the deposit.

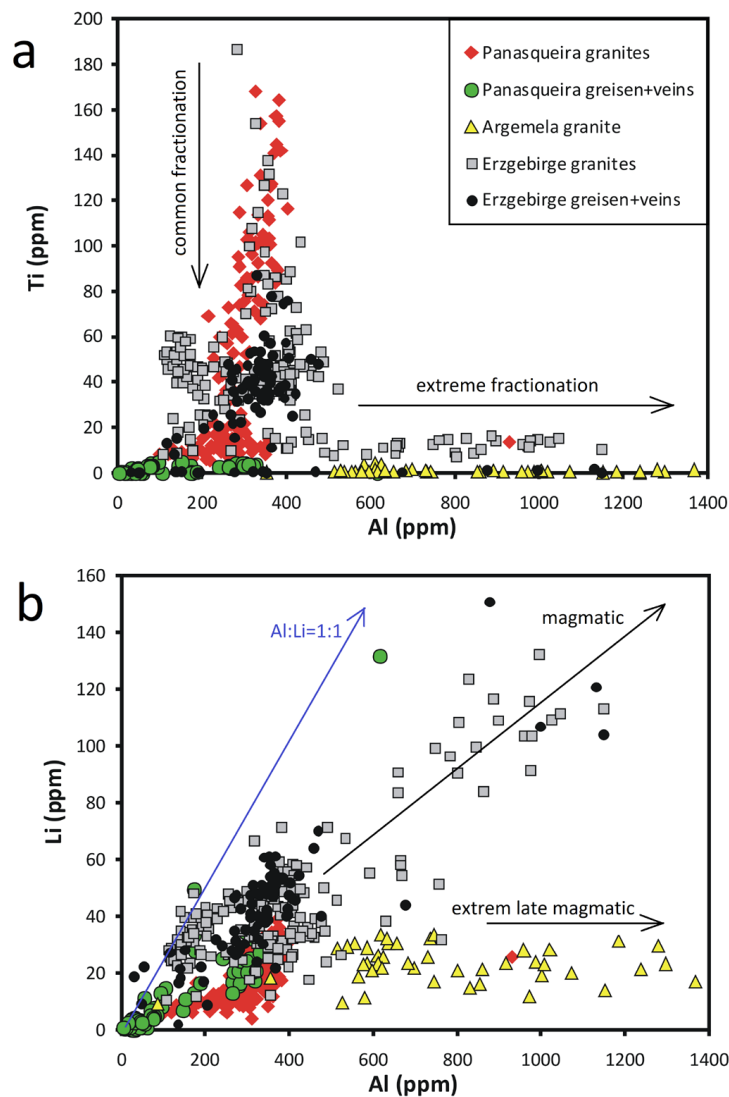


**Figure 18.** A comparison of trace elements in quartz from Panasqueira with those in quartz from Argemela [26] and the Erzgebirge (authors’ data): (a) Al vs. Ti; (b) Al vs. Li.

Lithium in quartz serves as a charge balancer for Al ( $\text{Al}^{3+} + \text{Li}^+$  for  $\text{Si}^{4+}$ ), being positioned in open channels in the quartz crystal structure [54]. Therefore, the atomic ratio of  $\text{Li}/\text{Al} = 1:1$  should be expected. Nevertheless, Li competes with  $\text{H}^+$  in this function, and real  $\text{Li}/\text{Al}$  values are lower (1:2 to 1:3) in common granites and also lower in extremely fractionated, although Li-rich leucogranites, such as Argemela. This probably results from the high content of water in the residual melt, implying a high activity of  $\text{H}^+$  (Figure 18b).

## 6. Conclusions

The Panasqueira pluton is of N–S-elongated elliptical shape that roughly covers an area of  $10 \times 5$  km and is composed of two phases: the older medium-grained porphyritic granite constitutes most of the pluton volume with a small cupola at Rio reaching 200–250 m a.s.l. Subordinate fine- to medium-grained leucogranite, dominantly forming the Panasqueira granite/greisen cupola, reaches ca. 650 m a.s.l. The upper part of the Panasqueira cupola was hydrothermally metasomatized to quartz–muscovite greisen, passing upwards to a nearly pure quartz cap connected with a swarm of sub-horizontal quartz–muscovite veins with disseminations of wolframite. In contrast, the cupola at Rio is only poorly greisenized and accompanied by only scarce quartz–wolframite veinlets.

Evolution of the bulk-rock geochemical indicators (decrease in the  $\text{Nb}/\text{Ta}$  and  $\text{Zr}/\text{Hf}$  values) and changes in the trace elements spectra of quartz and zircon (i.e., increase in the  $\text{Ge}/\text{Ti}$  and  $\text{Hf}/\text{Zr}$  values, respectively) support the existence of two intrusions connected via magmatic fractionation.

All mica varieties from Panasqueira are Li-poor; muscovite shows a strong positive Li–Fe correlation, indicating the substitution of  $\text{Li} + \text{Fe}$  for Al. The low  $\text{Nb}/\text{Ta}$  values and elevated Sn, W, Nb, and Ta contents illustrate the accumulation of these elements during the fractionation of magma and following magmatic/hydrothermal transition. Tungsten contents of 40–140 ppm W in muscovite from greisen are comparatively very high and can be possibly accepted as an indicator of W-laden fluids forming wolframite mineralization in more distal, cooler parts of the magmatic/hydrothermal system.

The Panasqueira granites and the associated greisens and quartz veins show similarity with the fairly fractionated Sn–W granites of the Erzgebirge, but they are distinct from the neighboring Argemela stock. This perhaps suggests common Sn–W mineralization processes across the Variscan belt in western and central Europe in close proximity to unmatched systems such as Argemela.

The Panasqueira pluton was a source of W for the large deposit, although it was not primarily W-richer than the majority of dominantly Sn-bearing RMGs across Variscan Europe. Our data suggest that there was no simple relationship between the rare metal contents in the parental magma and its ability to create an economic deposit. Spatial conditions of the magma emplacement, such as a cupola- or stock-like shape of the pluton apophyses that focus the flux of hydrothermal fluids, and suitable lithology of the country rocks, can play a decisive role.

**Author Contributions:** Conceptualization, field work, writing and editing—K.B.; methodology and data supervision—M.V.G.; data acquisition—J.Ď., Z.K. and M.H. All authors have read and agreed to the published version of the manuscript.

**Funding:** This study was supported by the Czech Science Foundation project No. P210/19/05198S and by RVO 67985831 at the Institute of Geology of the Czech Academy of Sciences. The cooperation of MVG and MH was supported by the Czech Science Foundation project EXPRO No. 19-29124X to BIC Brno.

**Data Availability Statement:** Original data are available at the authors on request.

**Acknowledgments:** The authors thank the staff of the Panasqueira mine in 2001 (Avocet Company, R.A. Naique) for all support during the field work. Almonty Industries, the current owner of the Panasqueira mine (Paulo Ferraz), is thanked for their kind permission to publish this contribution. Marek Dosbaba, Tescan Orsay Holding Brno, is thanked for providing TIMA mineral maps. Three anonymous reviewers are thanked for their constructive recommendations which helped us to improve the original manuscript.

**Conflicts of Interest:** The authors declare no conflict of interest.

## Appendix A

**Table A1.** List of boreholes reaching granite or greisen according to the Beralt documentation.

Borehole No.	Year of Realization	X	Y	Z	Max. Depth (m)	Core Fragments Preserved
1C	1952/53	31,814.9	54,560.98	530.09	272.6	no
12C	1956	35,578.62	51,205.84	378.85	156.18	no
28C	1964	32,220.79	54,605.52	679.03	150.4	no
29C	1964	32,258.83	54,718.54	619.3	90.35	no
30C	1966	32,047.38	54,563.2	528.7	82.26	in mine without depth localization
13D	1969/70	32,520.91	53,300.05	608.0	492.3	no
18D	1978/79	32,117.7	54,188.00	525.8	176.37	yes
9E	1959	31,913.3	54,727.09	531.1	143.33	no
12E	1957	31,973.59	54,851.43	621.4	91.02	no
14E	1959	31,961.47	54,816.89	531.2	108.5	no
34E	1971/72	32,846.6	54,536.3	796.9	361.92	yes
49E	1981/82	34,028.5	53,141.1	515.5	343.7	no
52E	1984	34,118.47	55,642.32	490.4	337.07	no
53E	1984/85	34,860.15	51,562.1	464.59	340.68	no
54E	1985	35,281.7	51,547.8	478.3	206.65	no
19F	1982	35,779.00	51,688.00	364.4	132.79	no
20F	1982	36,434.00	51,296.00	480.7	388.75	yes
3G	1980/81	32,882.00	53,231.84	559.87	417.6	yes
4G	1981	32,595.56	53,588.23	646.84	464.43	no
42L	1983	31,607.05	53,638.00	564.5	79.54	yes
32	1948	32,025.25	54,708.58	619.2	120.65	no
33	1948	32,129.3	54,683.4	618.8	75.3	no
54	1950	32,059.42	54,812.66	683.65	106.6	no
72	1951	32,047.49	54,970.05	621.36	85.95	no
73	1951	31,866.53	54,653.5	619.5	130.11	no
74	1951	31,822.42	54,577.63	619.35	143.3	no
75	1952	31,947.61	54,385.85	528.1	126.2	no
76	1952	31,695.47	54,388.56	528.52	100.64	no
77	1952	31,849.22	54,830.44	620.63	151.4	no
79	1952	31,915.65	54,944.4	621.5	137.56	no
80	1952	32,241.96	54,880.6	620.31	125.68	no

Table A1. Cont.

Borehole No.	Year of Realization	X	Y	Z	Max. Depth (m)	Core Fragments Preserved
81	1952	32,157.16	54,501.46	617.00	104.45	no
2N	1991	31,969.7	53,729.25	471.00	86.59	no
44M	1985	31,740.95	54,560.6	619.00	146.44	no
48M	1985	31,884.02	54,481.82	618.3	111.78	no
50M	1985	31,927.8	54,461.07	618.8	150.65	yes
55M	1985	31,727.6	54,317.4	563.21	130.03	yes
56M	1985/86	31,631.7	54,352.5	563.09	148.6	yes
74M	1990	32,036.49	53,853.15	470.9	114.8	no

Table A2. List of samples.

Sample	Localization	Description
1	Borehole 50M, 114.8–115.0 m	Ms-rich greisen
2	Borehole 50M, 117.6–117.8 m	Greisenized leucogranite
3	Borehole 18D, 150.2–150.4 m	Greisenized granite passed into mica-rich greisen
4	Borehole 18D, 156.0–156.2 m	Porphyritic granite
5	Borehole 18D, 156.8–157.0 m	Porphyritic granite
6	Borehole 18D, 157.8–157.9 m	Quartz-phosphate veinlets
7	Borehole 18D, 172.2–172.3 m	Greisenized granite
8	Mine, level 1, E-part of the cupola, 25 m to the E of the panel 4	Steep dike of the pink leucogranite through the greisen body
9	Mine, level 1, E-part of the cupola, 25 m to the E of the panel 4	Transition of the leucogranite to greisen
10	Mine, level 1, western contact of the cupola	Quartz-rich greisen with sulfides
11	Mine, level 1, E-part of the cupola, E of steep granite dike	Mica-rich greisen
12	Mine, level 1, 5 m to the W from the western contact of the cupola	Flat quartz vein, 15–20 cm thick, with micaceous jacket, disseminated cassiterite, small aggregates of wolframite, common sulfides
13	The same place as previous sample	Cassiterite-rich domain
14	The same place as previous sample	Wolframite-rich domain
15	Not localized, sample from the mineral shop	2 cm thick aggregate of white mica
16	Not localized, sample from the mineral shop	Piece of vein quartz with brown phosphate, white mica and arsenopyrite
17	Mine, level 3, D-18, R-1, AW30,	40 cm thick flat quartz vein with mica jackets
18	Mine, level 3, D-19, R-3, AW34,	The lower micaceous jacket of major quartz vein with small vugs with apatite crystals
19	Mine, level 3, D-19, R-3, AW34, 30–35 mm thick lower micaceous jacket of the 60 cm thick quartz vein	Mica crystallizing directly on the schist, small vugs with mica crystal were later filled with milky quartz
20	Mine, level 3, D-19, R-3, AW34,	Complete section of a 6 cm thick quartz vein with 10–15 mm thick micaceous rims. Scheelite and apatite inside.

Table A2. Cont.

Sample	Localization	Description
21	Mine, level 3, D-19, R-3, AW34,	Small wolframite chips from a 40–60 cm thick quartz vein
22	Rio, outcrop on the northern bank of the Rio Zezere, 9 m to the south of the bridge	Lower part of the steep 8 cm thick dike of greisenized aplite
23	Rio, outcrop on the northern bank of the Rio Zezere, 9 m to the south of the bridge	upper part of the steep 8 cm thick dike of greisenized aplite
28	Borehole 34E, 342.2–342.3 m	Weakly altered porphyritic granite, fresh feldspar crystals up to 10 × 4 mm, rich in white mica, no visible biotite
29	Borehole 50M, 118.4–118.6 m	Fine-grained muscovite leucogranite with disseminated pyrite
30	Borehole 50M, 123.4–123.6 m	Fine-grained, weakly greisenized leucogranite without sulfides
31	Borehole 56M, 132.4–132.5 m	Fine-grained leucogranite with local greisenization
32	Borehole 56M, 134.1–134.2 m	Fine-grained leucogranite, fresh
33	Borehole 3G, 356.6–356.8 m	Porphyritic granite with fine groundmass, feldspar grains up to 20 × 7 mm, quartz grains 5–10 mm across, accumulations of quartz, siderite, triplite and blue apatite
34	Borehole 3G, 355.9–356.0 m	Layered granite with oriented quartz and mica crystals (stockscheider)
35	Borehole 3G, 356.0–356.1 m	Layered granite below the stockscheider passing into greisenized granite
36	Borehole 3G, 358.2–358.3 m	Fine-grained mica-rich greisen
37	Borehole 3G, 362.1–362.2 m	Medium- to fine-grained leucogranite
38	Borehole 3G, 378.4–378.5 m	Contact granite/pegmatite dike
39	Borehole 20F, 239.4–239.5 m	Upper contact of granite body with thin stockscheider
40	Borehole 20F, 239.5–239.6 m	Fine-grained greisenized granite rich in mica, with strongly altered feldspars and disseminated pyrite
41	Borehole 20F, 262.6–262.7 m	Section through a thin granite dike with 2 cm stockscheider along the upper contact
42	Borehole 20F, 372.9–373.0 m	Fresh porphyritic granite with white 15 × 10 mm feldspars, 5 mm rounded quartz and medium-grained matrix
43	Borehole 20F, 379.2–379.4 m	Greisenized medium-grained porphyritic granite, feldspars strongly altered, disseminated pyrite
44	Borehole 42L, 35.5 m	2 cm thick micaceous vein within schist
45	Borehole 3G, 359.0–359.2 m	Fine-grained weakly greisenized granite with irregular texture
46	Mine, level 530 m, panel 2-north, short crosscut to the west	Quartz-rich greisen with sulfide dissemination near a steep quartz-wolframite vein
47	Mine, level 530 m, panel 2-north, 25 m from the end of the panel, western wall	Enclave of fresh granite within greisen body, medium- to fine-grained granite, pink feldspars, white mica
48	Mine, the same place	Greisen with disseminated sulfides
49	Mine, level 530 m, panel 2-north, 5 m from the end of the panel, western wall	Enclave of white greisenized granite within greisen
50	Mine, level 530 m, borehole 30C on the north end on the panel 2, unlocalized fragments of the core on the original borehole place	Fine-grained leucogranite

Table A2. Cont.

Sample	Localization	Description
51	The same place	Weakly greisenized leucogranite rich in muscovite
52	The same place	Weakly altered porphyritic granite with feldspars up to 10 × 5 mm
53	The same place	Fine- to medium-grained two-mica granite with quartz grains up to 5 mm across
54	Eastern slope of the valley between St. Francisco and Rio, NW-part of the greisen vein indicated by Thadeu	Blocks of fine-grained greisenized granite with disseminated arsenopyrite and small vugs filled with quartz and white mica crystals
55	Old stope on the eastern slope of the valley between St. Francisco and Rio, central part of the greisen vein indicated by Thadeu, outcrop	Steep 20 cm thick quartz vein with ca. 10 cm thick rim of greisenized granite along the E-contact

## References

- Thadeu, D.C. Geologia de couro mineiro da Panasqueira. *Com. Serv. Geol. Portugal* **1951**, *32*, 5–64.
- Bloot, C.; de Wolf, L.C.M. Geological features of the Panasqueira tin-tungsten ore-occurrence (Portugal). *Bolet. Soc. Geol. Portugal* **1953**, *11*, 1–58.
- D'Orey, F.C. Tungsten-tin mineralization and paragenesis in the Panasqueira and Vale de Ermida mining districts, Portugal. *Com. Serv. Geol. Portugal* **1967**, *52*, 117–167.
- Kelly, W.C.; Rye, R.O. Geologic, fluid inclusion and stable isotope studies of the tin-tungsten deposits of Panasqueira, Portugal. *Econ. Geol.* **1979**, *74*, 1721–1822. [[CrossRef](#)]
- Bussink, R.W. Geochemistry of the Panasqueira Tungsten-Tin Deposit, Portugal. Ph.D. Thesis, Instituut voor Aardwetenschappen der Rijksuniversiteit te Utrecht, Utrecht, The Netherlands, 1984.
- Oosterom, M.G.; Bussink, R.W.; Vriend, S.P. Lithogeochemical studies of aureoles around the Panasqueira tin-tungsten deposit, Portugal. *Miner. Dep.* **1984**, *19*, 283–288. [[CrossRef](#)]
- Foxford, K.A.; Nicholson, R.; Polya, D.A. Textural evolution of W-Cu-Sn-bearing hydrothermal veins at Minas da Panasqueira, Portugal. *Min. Mag.* **1991**, *55*, 435–445. [[CrossRef](#)]
- Neiva, A.M.R. Portuguese granites associated with Sn-W and Au mineralizations. *Bull. Geol. Soc. Finl.* **2002**, *74*, 79–101. [[CrossRef](#)]
- Breiter, K. *Report about Laboratory Investigations of Rock Samples from the Panasqueira Mine and Recommendation for Future Exploration*; Manuscript; Beralt Co.: Panasqueira, Portugal, 2001.
- Pinto, F.M.V. Estudo da distribuicao do Estanho na mina da Panasqueira. Master's Thesis, Porto University, Porto, Portugal, 2007.
- Pinto, F.; Vieira, R.; Noronha, F. Different cassiterite generations at the Panasqueira deposit (Portugal): Implications for the metal zonation model. In *Mineral Resources in Sustainable World, Proceedings of the 13th SGA Biennial Meeting, Nancy, France, 24–27 August 2015*; The Society for Geology Applied to Mineral Deposits (SGA): Geneva, Switzerland, 2015; Volume 2, pp. 827–830.
- Goncalves, M.A.; Mateus, A.; Pinto, F.; Vieira, R. Using multifractal modelling, singularity mapping, and geochemical indexes for targeting buried mineralization: Application to the Panasqueira ore-system, Portugal. *J. Geoch. Explor.* **2018**, *189*, 42–53. [[CrossRef](#)]
- Carocci, E.; Marignac, C.; Cathelineau, M.; Truche, L.; Lecomte, A.; Pinto, F. Rutile from Panasqueira (Central Portugal): An excellent pathfinder for wolframite drposition. *Minerals* **2019**, *9*, 9. [[CrossRef](#)]
- Codeco, M.S.; Weis, P.; Trumbull, R.; Glodny, J.; Wiedenbeck, M.; Romer, R.L. Boron isotope muscovite-tourmaline geothermometry indicates fluid cooling during magmatic-hydrothermal W-Sn ore formation. *Econ. Geol.* **2019**, *114*, 153–163. [[CrossRef](#)]
- Mateus, A.; Figueiras, J.; Martins, I.; Reis, P.C.; Pinto, F. Relative abundance and compositional variation of silicates, oxides and phosphates in the W-Sn-rich lodes of the Panasqueira Mine (Portugal); implications to the ore-forming process. *Minerals* **2020**, *10*, 551. [[CrossRef](#)]
- Launay, G.; Sizaret, S.; Guillou-Frottier, L.; Gloaguen, E.; Pinto, F. Deciphering fluid flow at the magmatic-hydrothermal transition: A case study from the world-class Panasqueira W-Sn-(Cu) deposit (Portugal). *Earth Planet. Sci. Lett.* **2018**, *499*, 1–12. [[CrossRef](#)]
- Launay, G.; Sizaret, S.; Lach, P.; Melleton, J.; Gloaguen, E.; Poujol, M. Genetic relationship between greisenization and Sn-W mineralizations in vein and greisen deposits: Insights from the Panasqueira deposit (Portugal). *BSGF—Earth Sci. Bull.* **2021**, *192*, 2. [[CrossRef](#)]
- Noronha, F.; Dória, A.; Dubessy, J.; Charoy, J. Characterization and timing of the different types of fluids present in the barren and ore-veins of the W-Sn deposit of Panasqueira. *Miner. Dep.* **1992**, *27*, 72–79. [[CrossRef](#)]
- Lourenco, A. O granite da Panasqueira (Cúpola da Barro Grande). Estudo de um Sistema granítico associado a mineralizacoes de estanho. In *Proceedings of the VII Congresso Nacional de Geologia, University Évora, Évora, Portugal, 5 July 2006*; pp. 187–190.

20. Marignac, C.; Cuney, M.; Cathelineau, M.; Lecomte, A.; Carocci, E.; Pinto, F. The Panasqueira rare metal granite suites and their involvement in the genesis of the world-class Panasqueira W-Sn-Cu deposit: A petrographic, mineralogical, and geochemical study. *Minerals* **2020**, *10*, 562. [[CrossRef](#)]
21. Portugal-Ferreira, M.; Costa, V.; Macedo, C.R.; Pereira, L.G. Datacoes K-Ar em biotite das rochas granitoides da Cova da Beira (Portugal Central). *Mem. Not. Mus. Lab. Min. Geol. Univ. Coimbra* **1977**, *84*, 39–48.
22. Neiva, A.M.R.; Neiva, J.M.C.; Parry, S.J. Geochemistry of the granitic rocks and their minerals from Serra da Estrela, Central Portugal. *Geochim. Cosmochim. Acta* **1987**, *51*, 439–454. [[CrossRef](#)]
23. Charoy, B.; Noronha, F. Multistage growth of a rare-element, volatile-rich microgranite at Argemela (Portugal). *J. Petrol.* **1996**, *37*, 73–94. [[CrossRef](#)]
24. Michaud, J.A.S.; Gumiaux, C.; Pichavant, M.; Gloaguen, E.; Marcoux, E. From magmatic to hydrothermal Sn-Li-(Mn-Ta-W) mineralization: The Argemela area (central Portugal). *Ore Geol. Rev.* **2020**, *116*, 103215. [[CrossRef](#)]
25. Lima, L.; Guedes, A.; Noronha, F. Tungsten mineralization associated to Argemela microgranite (Central Portugal). *J. Iber. Geol.* **2019**, *45*, 625–640. [[CrossRef](#)]
26. Breiter, K.; Ďurišová, J.; Korbelová, Z.; Lima, A.; Vašinová Galiová, M.; Hložková, M.; Dosbaba, M. Rock textures and mineral zoning—A clue to understanding rare-metal granite evolution: Argemela stock, Central-Eastern Portugal. *Lithos* **2022**, *410–411*, 106562. [[CrossRef](#)]
27. Ribeiro, R.F. Gravimetric Modelling and Geological Interpretation of Argemela–Panasqueira Area. Master’s Thesis, Porto University, Porto, Portugal, 2017.
28. Shannon, J.R.; Walker, B.M.; Carten, R.B.; Geraghty, E.P. Unidirectional solidification textures and their significance in determining relative ages of intrusions at the Henderson Mine, Colorado. *Geology* **1982**, *10*, 293–297. [[CrossRef](#)]
29. Breiter, K. From explosive breccia to unidirectional solidification textures: Magmatic evolution of a phosphorus- and fluorine-rich granite system (Podlesí, Krušné hory Mts., Czech Republic). *Bull. Czech Geol. Surv.* **2002**, *77*, 67–92.
30. Hrstka, T.; Gottlieb, P.; Skála, R.; Breiter, K.; Motl, D. Automated mineralogy and petrology—Applications of TESCAN Integrated Mineral Analyzer (TIMA). *J. Geosci.* **2018**, *63*, 47–63. [[CrossRef](#)]
31. Jochum, K.P.; Weis, U.; Stoll, B.; Kuzmin, D.; Yang, Q.; Raczek, I.; Jacob, D.E.; Stracke, A.; Birbaum, K.; Frick, D.A.; et al. Determination of reference values for NIST SRM 610–617 glasses following ISO guidelines. *Geostand. Geoanal. Res.* **2011**, *35*, 397–429. [[CrossRef](#)]
32. Breiter, K.; Ďurišová, J.; Dosbaba, M. Chemical signature of quartz from S- and A-type rare-metal granites—A summary. *Ore Geol. Rev.* **2020**, *125*, 103674. [[CrossRef](#)]
33. Flem, B.; Bédard, L.P. Determination of trace elements in BCS CRM 313/1 (BAS) and NIST SRM 1830 by inductively coupled plasma-mass spectrometry and instrumental neutron activation analysis. *Geostand. Newslett.* **2002**, *26*, 287–300. [[CrossRef](#)]
34. McDonough, W.F.; Sun, S. The composition of the Earth. *Chem. Geol.* **1995**, *120*, 223–253. [[CrossRef](#)]
35. Larsen, R.B.; Henderson, I.; Ihlen, P.M.; Jacamon, F. Distribution and petrogenetic behavior of trace elements of granitic quartz from South Norway. *Contrib. Mineral. Petrol.* **2004**, *147*, 615–628. [[CrossRef](#)]
36. Monier, G.; Robert, J.L. Evolution of the miscibility gap between muscovite and biotite solid solutions with increasing lithium content: An experimental study in the system K<sub>2</sub>O–Li<sub>2</sub>O–MgO–FeO–Al<sub>2</sub>O<sub>3</sub>–SiO<sub>2</sub>–H<sub>2</sub>O–HF at 600 °C, 2 kbar PH<sub>2</sub>O: Comparison with natural lithium micas. *Min. Mag.* **1986**, *50*, 641–651. [[CrossRef](#)]
37. Stepanov, A.; Mavrogenes, J.A.; Meffre, S.; Davidson, P. The key role of mica during igneous concentration of tantalum. *Contrib. Mineral. Petrol.* **2014**, *167*, 1009. [[CrossRef](#)]
38. Foster, M.D. Interpretation of the composition of lithium micas. *U.S. Geol. Surv. Prof. Pap.* **1960**, *354-E*, 115–147.
39. London, D.; Morgan, G.B., VI; Babb, H.A.; Loomis, J.L. Behaviour and effect of phosphorus in system Na<sub>2</sub>O–K<sub>2</sub>O–Al<sub>2</sub>O<sub>3</sub>–SiO<sub>2</sub>–P<sub>2</sub>O<sub>5</sub>–H<sub>2</sub>O at 200 MPa (H<sub>2</sub>O). *Contrib. Mineral. Petrol.* **1993**, *113*, 450–465. [[CrossRef](#)]
40. Breiter, K.; Frýda, J.; Leichmann, J. Phosphorus and rubidium in alkali feldspars: Case studies and possible genetic interpretation. *Bull. Czech Geol. Surv.* **2002**, *77*, 93–104.
41. Piccoli, P.M.; Candela, P.A. Apatite in igneous system. *Rev. Mineral. Geochem.* **2019**, *48*, 255–292. [[CrossRef](#)]
42. Breiter, K.; Förster, H.-J.; Škoda, R. Extreme P-, Bi-, Nb-, Sc-, U- and F-rich zircon from fractionated perphosphorus granites: The peraluminous Podlesí granite system, Czech Republic. *Lithos* **2006**, *88*, 15–34. [[CrossRef](#)]
43. Breiter, K.; Müller, A.; Shail, R.; Simons, B. Composition of zircons from the Cornubian Batholith of SW England and comparison with zircons from other European Variscan rare-metal granites. *Min. Mag.* **2016**, *80*, 1273–1289. [[CrossRef](#)]
44. Zaraisky, G.P.; Aksyuk, A.M.; Devyatova, V.N.; Udoratina, O.V.; Chevychelov, V.Y. The Zr/Th ratio as a fractionation indicator of rare metal granites. *Petrology* **2009**, *17*, 25–45. [[CrossRef](#)]
45. Breiter, K.; Škoda, R. Zircon and whole-rock Zr/Hf ratios as markers of the evolution of granitic magmas: Examples from the Teplice caldera (Czech Republic/Germany). *Mineral. Petrol.* **2017**, *111*, 435–457. [[CrossRef](#)]
46. Lecumberri-Sanchez, P.; Vieira, R.; Heinrich, C.A.; Pinto, F.; Wälle, M. Fluid-rock interaction is decisive for the formation of tungsten deposits. *Geology* **2017**, *45*, 579–582. [[CrossRef](#)]
47. Ballouard, C.; Pojol, M.; Boulvais, P.; Branquet, Y.; Tartese, R.; Vigneresse, J.-L. Nb-Ta fractionation in peraluminous granites: A marker of the magmatic-hydrothermal transition. *Geology* **2016**, *44*, 231–234. [[CrossRef](#)]
48. Breiter, K.; Korbelová, Z.; Vašinová Galiová, M.; Hložková, M. Micas from the rare metal granites. *Lithos*, 2023; *under review*.

49. Michaud, J.; Pichavant, M. The H/F ratio as an indicator of contrasted wolframite deposition mechanism. *Ore Geol. Rev.* **2019**, *104*, 266–272. [[CrossRef](#)]
50. Rudnick, R.L.; Gao, S. Composition of the continental crust. *Treatise Geochem.* **2003**, *3*, 1–64.
51. Müller, A.; Seltman, R.; Halls, C.; Siebel, W.; Dulski, P.; Jeffries, T.; Spratt, J.; Kronz, A. The magmatic evolution of the Land's End pluton, Cornwall, and associated pre-enrichment of metals. *Ore Geol. Rev.* **2006**, *28*, 329–367. [[CrossRef](#)]
52. Breiter, K.; Ďurišová, J.; Hrstka, T.; Korbelová, Z.; Vašinová Galiová, M.; Müller, A.; Simons, B.; Shail, R.K.; Williamson, B.J.; Davies, J.A. The transition from granite to banded aplite-pegmatite sheet complexes: An example from Megiligar Rocks, Tregonning topaz granite, Cornwall. *Lithos* **2018**, *302–303*, 370–388. [[CrossRef](#)]
53. Štemprok, M.; Pivec, E.; Langrová, A. The petrogenesis of a wolframite-bearing greisen in the Vykmanov granite stock, Western Krušné hory pluton (Czech Republic). *Bull. Geosci.* **2005**, *80*, 163–184.
54. Götze, J.; Möckel, R. (Eds.) *Quartz: Deposits, Mineralogy and Analytics*; Springer: Berlin, Germany, 2012; pp. 1–360.
55. Breiter, K.; Müller, A. Evolution of rare-metal granitic magmas documented by quartz chemistry. *Europ. J. Mineral.* **2009**, *21*, 335–346. [[CrossRef](#)]
56. Ďurišová, J. Origin of greisen assemblages in the western Krušné hory Mts. *Věst. Ústř. Úst. Geol.* **1984**, *59*, 141–152.
57. Korges, M.; Weis, P.; Lüders, V.; Laurent, O. Depressurization and boiling of a single magmatic fluid as a mechanism for tin-tungsten deposit formation. *Geology* **2018**, *46*, 75–78. [[CrossRef](#)]

**Disclaimer/Publisher's Note:** The statements, opinions and data contained in all publications are solely those of the individual author(s) and contributor(s) and not of MDPI and/or the editor(s). MDPI and/or the editor(s) disclaim responsibility for any injury to people or property resulting from any ideas, methods, instructions or products referred to in the content.